Spicules

Master thesis by
Silje Bjølseth
Institute of Theoretical Astrophysics
University of Oslo
Norway

November 2008

Takk

Aller først ønsker jeg å gi en stor takk til prof. Mats Carlsson for kyndig veiledning, stor tålmodighet og for alltid å ha hatt tid til meg. Videre ønsker jeg å takke Øystein Langangen for hjelp til stort og smått, og for å snu mine negative tanker til positive Takk også til Kosovare Olluri for godt samarbeid med å pløye gjennom Hinodes formidable data-arkiv.

En stor takk også til alle dere som har fylt studietilværelsen min med minner for livet. DreamTeam Inc. (Kristin, Michael og Espen) for faglige diskusjoner som har vært uunnværlige for å overleve faglig sett, og de mange sprellene som har vært uunnværlig for å overleve livet ellers.

Zoya for å gi meg mot til å bli med i studentutvalget og for alle de gode (og ikke minst de fjasete) samtalene og shoppingturer når studiene tynget og vi trengte å avkoble med noe helt annet.

Anita og Nina for alle de små avbrekkene som gjorde de lange (og de korte) dagene på lesesalen levelige.

Alle i Studentorchesteret Biørneblæs for musikken, sangene, festene, turene og alt det andre vi har funnet på. Livet mitt ville ha vært fattigere uten dere.

Og sist, men definitivt ikke minst, en kjempestor takk til Eivind. Uten deg ville ikke denne masteroppgaven ha eksistert. Din støtte og omtanke har vært utrolig viktig for meg. Du er Solen i mitt liv.

Silje Bjølseth
Oslo, November 7, 2008

Hinode is a Japanese mission developed and launched by ISAS/JAXA, with NAOJ as domestic partner and NASA and STFC (UK) as international partners. It is operated by these agencies in co-operation with ESA and NSC (Norway).

Contents

List of Figures

List of Tables

Chapter 1

Introduction

In the beginning the Universe was created. This has made a lot of people very angry and has been widely regarded as a bad move.

–Douglas Adams

1.1 Outline of the thesis

The Sun is a constant cause of scientific research. There are still many things we do not know about our closest star. Knowing how the Sun works is important both because of the direct impact it has on everyday life on the Earth and as a means to understand stars in general.

The Sun has a large atmosphere classically divided into four layers. One of these layers is the chromosphere. It has recently become more and more evident that the chromosphere is very dynamic and not just a homogenic layer as it has often been described as being. New and more powerful solar telescopes have for the past two decades given us valuable insight on the chromosphere. The temperature within the chromosphere varies a lot more than earlier presumed, and stuctures in the chromosphere are more dynamic. One of these structures is known as *spicules*, and they are the main object of research in this thesis.

In addition to better telescopes, there has also been a huge development in computer science, making it easier and faster to deal with large amounts of data from the telescopes.

Observations used in this thesis were done using the Japanese satellite Hinode, described in Section 3.1. Hinode's main goal is to shed light on how the lower layers of the solar atmospheres affect the higher layers. By using Hinode, we can hopefully learn new things about the chromosphere in general and particularily spicules. Spicules are thin and extend a few thousand kilometres above the Sun's surface. They have a short lifespan (down to a few tens of seconds), and appear and disappear very rapidly. They seem to follow the field lines of the magnetic field and it appears that

matter is transported outwards along them with speeds of tens of kilometres per second. It is expected that when spicules are better understood, they can give us new insights into the energy and mass balances in the chromosphere as well as teach us about the magnetic structure.

1.1.1 Main goals

This thesis aims to use observations made with Hinode to characterize spicules, and to measure their lifespans, velocities and differences between different regions (quiet Sun, plage, corona holes).

The tools that will be used are software packages developed at the Institute of Theoretical Astrophysics (ITA), University of Oslo, and other places for treatment of Hinode data.

In Chapter 1, the theoretical background is described. The Sun's atmosphere and particularly the chromosphere with its dynamic structures are explained, and a quick background on acoustic waves is given.

In Chapter 2 the theories of electromagnetic radiation and radiative transfer as applied in solar physics are described.

In Chapter 3, the methods and techniques used in the thesis are described. There is a section on the Hinode satellite and descriptions of the most important instruments for this thesis. There are also sections on important issues in observational astronomy. Furthermore, the data reduction process is explained.

In Chapter 4, the results of the thesis are laid out, and finally, in Chapter 5, the results are discussed and conclusions are made.

1.2 The solar atmosphere

The solar atmosphere can be divided into four layers: The photosphere, the chromosphere, the transition layer and the corona. These layers are mainly divided on the basis of their temperatures.

The *photosphere*, the visible surface of the Sun, has a temperature between 5000 and 6000 Kelvin. It is characterized by granulation patterns and sunspots, and is only about 0.5 Mm thick. The photosphere is where the solar gas changes from being completely opaque to becoming almost completely transparent (in visible light), i.e. where the solar atmosphere becomes optically thin. Almost all the light we recieve from the Sun originates in the photosphere. Luckily for us, the optical depth (the depth from which the light we see originates) depends on both position on the Sun and the wavelength of the light, making it possible for us to observe the solar atmosphere at different depths. There are several strong spectral line states that are still opaque high up in the atmosphere (spectral lines will be explained in Chapter 2). This is how we can observe the next layers in the solar atmosphere.

Outside the photosphere lies the *chromosphere*, which extends about 2 Mm outwards and has a temperature of around 8000 Kelvin. The chromosphere is optically thin at most wavelengths and is thus not easily observable in visible light due to the photosphere's brightness. Broadband imaging of the chromosphere is only easily done during eclipses, when the photosphere's light is blocked by the Moon. The chromosphere is most often recorded with narrow-band filters, that only samples a small wavelength area, usually centered around a strong spectral line, and which greatly enhances the chromospheric structures.

Above the chromosphere the temperature increases rapidly over only a few hundred kilometers before finally reaching a temperature of millions of Kelvin. This is known as the *transition region*. Above the transition region lies the *corona*. It extends into space for several solar radii, and has a temperature of a few million Kelvin. (See e.g. Carroll and Ostlie (1996) or any other undergraduate introduction to astrophysics literature.)

For a plot of the temperature distribution in the solar atmosphere, see Figure 2.3. This temperature distribution was derived with a model of the quiet Sun.

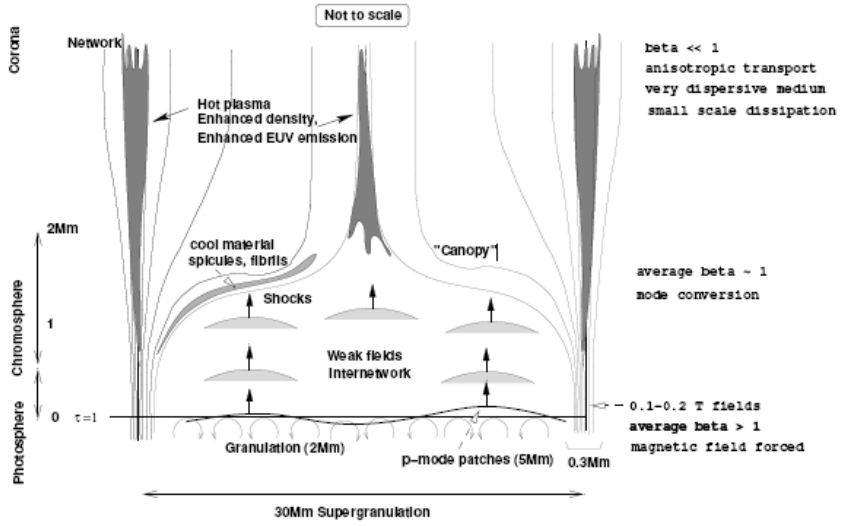

Figure 1.1: Outline of the quiet chromosphere's magnetic structure, from Judge (2006).

1.2.1 The chromosphere

The chromosphere is usually defined to begin at the height where the temperature rises after reaching a minimum in the outer photosphere of about

4400 K. It is highly dynamic, with variations down to a few tens of seconds. From the temperature minimum and upwards to about halfway into the chromosphere (at 1.5 Mm), the chromosphere is practically isothermal (i.e. the temperature is constant). At this height lies the "magnetic canopy", dividing the lower, weakly magnetized chromosphere from the higher, completely magnetized chromosphere (see Figure 1.1). At the canopy, the gas pressure equals the magnetic pressure, i.e. $\beta = 8\pi p/B^2 = 1$.

In the lower chromosphere, the magnetic field is concentrated in magnetic flux tubes, which originate in the photosphere's "intergranular network", i.e. the magnetic network in the photosphere which seperates the granules (where hot gas rises to the surface). The magnetic flux tubes are mainly vertical, and because they are in equilibrium with the surrounding gas, they expand upwards in order to conserve the magnetic flux (as the gas density decreases with height). In the photosphere they fill less than 1% of the the volume expanding to 15% in the lower chromosphere and further to 100% in the upper chromosphere (Hasan (2008)). The quiet Sun outside the network of magnetic flux tubes is called the internetwork or cell interior.

Observing the chromosphere

The chromosphere, as mentioned above, is optically thin at most wavelengths, but there are a few important strong spectral lines originating in the chromosphere, such as Hα and the Ca II H and K lines. (For more on spectral lines see Section 2.1 below). In this thesis the observations have been made in the Ca II H-line which primarily originates in the chromosphere, such as spicules. One important method for observing the chromosphere is looking at the limb in one of these spectral lines. Limb observations reveal the basic chromospheric structures and some of their properties such as their height.

1.2.2 Coronal holes

Coronal holes are regions in the Sun's corona where the density is very low, around a hundred times less than that of the rest of the corona. Coronal holes are associated with areas where the magnetic field lines of the Sun are open, stretching out into space. That is why there are continous coronal holes above the poles, but they can also appear at other places in the Sun's corona. In X-ray images, coronal holes appear as dark voids, i.e. areas of low emission.

At lower latitudes, the frequency of coronal holes is at its lowest during solar minimum and at its highest during solar maximum (Ikhsanov and Ivanov (1999)). Here they are also more dynamic structures, appearing, growing and disappearing over the course of months. Some coronal holes may also move towards the poles to merge with the polar coronal holes.

In this thesis the effects of coronal holes on spicules are investigated.

1.2.3 Acoustic waves

Oscillations on the Sun were first reported in the 1960s and have since been thouroghly studied (Stix (2002)). These waves are generated by turbulence in the Sun's convection zone and are divided into different categories depending on the restoring force that drives them.

Acoustic or p-mode waves have pressure as their restoring force. P-modes have been observed with periods of 2-15 minutes, with five-minute oscillations being perhaps the most important ones. As well as being able to give us insight into how the solar interior is (the field of "helioseismology"), solar oscillations may also be important as a driving mechanism for depositing energy in the solar atmosphere.

In the lower part of the photosphere the p-mode waves are evanescent and cannot necessarily propagate further out into the atmosphere through the temperature minimum. The temperature minimum acts as a boundary that stops the p-mode waves from propagating through it, since the p-mode waves have longer periods than the local acoustic cut-off period. The acoustic cut-off period is given by

$$P_{ac} = \frac{4\pi c_s}{\gamma g}, \tag{1.1}$$

where c_s is the local speed of sound, γ is the ratio of specific heats and g is the effective gravity $g = g_0 \cos\theta$ (De Pontieu et al. (2004), Suematsu (1990)). In general, for the waves to be able to propagate through the boundary, they need to have periods lower than the cut-off.

Michalitsanos (1973) and Bel and Leroy (1977) looked at how the inclination angle θ of the magnetic field with the vertical can aid the p-mode waves in propagating outwards. They found that if the plasma can only travel along the magnetic field lines, the gravity will have a reduced effect, $g_0 \cos\theta$, on the plasma where $g_0 = 274$ km s^{-2} is the radial gravity. If the effective gravity is reduced, the cut-off period will be higher, which will then let waves with longer periods propagate outwards.

De Pontieu et al. (2004) also showed with simulations that it is possible for a wave to tunnel its energy through the temperature minimum and into the chromosphere, where the energy will yet again be able to propagate outwards due to the increasing temperature. The simulations also showed how inclination angles, θ, that deviates from the vertical will increase the possibility for this type of tunneling.

Acoustic waves propagating upwards can quickly turn into shocks, since the density in the chromosphere decreases rapidly with height. Shock waves have generally an "N" or "sawtooth" shaped velocity profile (Mihalas and Weibel-Mihalas (1999)). When a shock wave propagating outwards hit plasma, the plasma will gain a sudden impuls in velocity followed by a linear

deceleration when the shock retreats. This will give the velocity a parabolic path with time.

The role of acoustic waves in respect to this thesis will be discussed further in Chapter 4.

1.3 Spicules

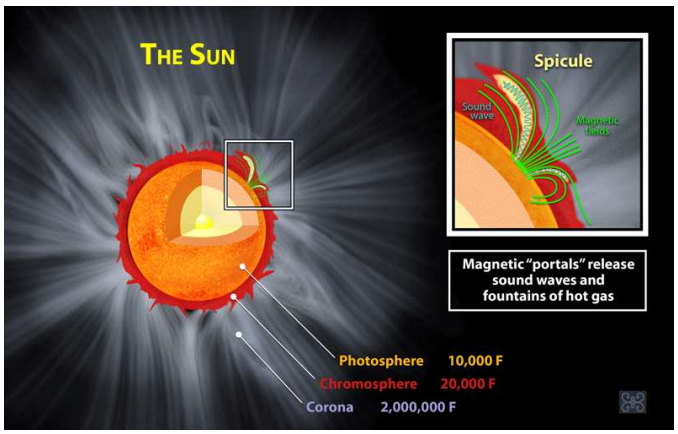

Figure 1.2: Illustration of the Sun's atmospheric layers and spicules (Courtesy of NASA/NSF).

The magnetic areas in the chromosphere off the limb of the Sun are dominated by highly dynamic, jet-like structures with a short lifespan. These are called spicules. See Figure 1.2 for a schematic view of the Sun with spicules and Figure 1.3 for an image of spicules as observed by Hinode.

There are other structures which are also jet-like, called dynamic fibrils and mottles, observed only on the disk. Dynamic fibrils are visible in and around plage areas (areas with strong magnetic field that result in a higher temperature and brightness than the surrounding areas) in active regions on the Sun. Mottles are areas coinsiding with strong magnetic field. They cover the entire Sun, both active and quiet regions. Coarse mottles are bright, often elongated and merge to form plages. Fine mottles are smaller, either dark or bright and have been theorized to be the disk equivalent of spicules.

Spicules have been the source of studies for more than a century, but there are still many unanswered questions about them that have been difficult to answer because spicules are so small that they long have bordered on the observational resolution limits. Due to relatively new and larger solar telescopes such as the ground based 1 meter Swedish Solar Telescope on La Palma and the SOHO, TRACE and Hinode spacecrafts, resolution limits are

no longer a problem.

One of the important questions that remain is to which extent spicules are related to mottles and dynamic fibrils.

Spicules sometimes appear in groups, "rosettas", where they appear to originate from a local concentration of magnetic fields in the photosphere.

Visual studies of spicules with Hinode (De Pontieu et al. (2007b)) have shown that there are two different populations of spicules with somewhat different properties, named type I and type II spicules. The main property in which they differ are their lifetimes. De Pontieu et al. (2007b) used Fourier-filtered time series to filter out the two different types.

The existence of two different populations of spicules is an indication that there are several different mechanisms driving the spicules.

1.3.1 Spicules type I

The structures traditionally known just as "spicules" are elongated, tilted structures in the chromosphere. They have an observed thickness of between 0.7 and 1.4 Mm (1 and 2 arcseconds), extend about 7-9 Mm out from the photosphere and seem to last between 3 and 7 minutes. The matter seen moving along the spicules is typically moving at speeds of 25 km/s, but speeds up to 70 km/s have been measured. (See for example Foukal (2004), Beckers (1968)).

Spicules type I dominate the limb in areas of active regions, but are more absent from quiet Sun and coronal holes.

A spicule of type I moves so that its tip has a parabolic path with time, first moving outwards and then falling back towards the solar surface. The deceleration of the spicule often differs from the contribution made by the Sun's gravity (274 m s^{-2} at the equator), with decelerations between 50 m s^{-2} and 400 m s^{-2}. These values are similar to those observed for dynamic fibrils from active regions and from some mottles in the quiet Sun. The linear correlation between the deceleration and maximum velocity for spicules type I is also identical to that of dynamic fibrils and mottles (De Pontieu et al. (2007b)).

This has led to the conclusion that type I spicules are driven by shock waves due to global oscillations and convective flows that leak into the upper atmosphere along tilted magnetic field lines, where they create shocks that drive the jets upwards (Hansteen et al. (2006), De Pontieu et al. (2007b)).

1.3.2 Spicules type II

Type II spicules are much thinner and more dynamic than type I, which is why there have not been any good observations of them until recently De Pontieu et al. (2007b). They have a typical lifetime of 10-150 seconds, have a thickness of less than 200 kilometres (down to the resolution limits of

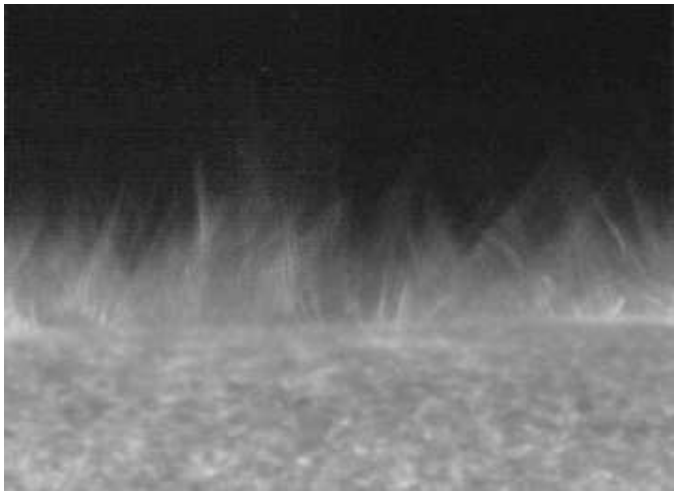

Figure 1.3: Spicules photographed by Hinode.

today's telescopes), lengths between 1 and 7 Mm and have outward velocities on the order of 50-150 km s^{-1}. They seem to have longer lifetimes in coronal holes, with a mean lifetime of 45 seconds, as opposed to 35 seconds for other areas.

Spicules type II have considerably higher velocities than type I, and unlike type I they do not seem to fall back into the photosphere, perhaps because they fade from view before they typically could be seen to fall back. The quick fading of spicules type II from calcium may be because the calcium-ions are ionised once more due to rapid heating. This would suggest transistion layer temperatures of at least 10^5 K.

By looking at space-time plots of spicules type II, it seems like the velocities are lower far down and are accelerated as they move upwards. They also have a considerable transversal motion, making it seem like they are swaying back and forth.

Spicules type II dominate coronal holes, where they also stretch further out into space, with typical heights of 5 Mm or more. In active regions they are shorter, especially when viewed on the disk, often with heights of no more than 1-2 Mm. In quiet Sun regions the spicules reach several Mm in height.

Chapter 2

Radiation

Everything should be made as simple as possible, but not simpler.
–Albert Einstein

To understand and interpret images of any astronomical object, it is important to understand how electromagnetic radiation occurs and how it is modified by matter. Electromagnetic radiation is a form of energy generated by acceleration of electrically charged particles (for example electrons or ions). Electromagnetic radiation has a wave-particle duality, making it possible to view the radiation as both waves and particles (called photons).

Electromagnetic waves consist of oscillating electric and magnetic fields positioned at right angles to each other and to the direction of travel. When moving through vacuum the relation between the speed (c), frequency (f) and wavelength (λ) of a wave is $c = f\lambda$.

Electromagnetic waves may also be viewed as a stream of photon particles with zero mass. The energy of a photon is related to the frequency by Planck's formula, $E = hf$, where h is Planck's constant and f is the frequency. This relation shows that the higher the frequency a photon has, the higher its energy is.

In this Chapter some of the key concepts behind understanding radiation and its transfer through matter are described, beginning with how spectral lines form and may give valuable information in Section 2.1, and continuing with radiative transfer in the solar atmosphere in Section 2.2. A little background information on computer simulations of the solar atmosphere is also given.

2.1 Line formation

Through interaction with matter, electromagnetic radiation will be modified, thus giving us information of the matter and the physical conditions in and around it. Radiation may be absorbed or emitted by the matter, or the path

of the wave/particle may be deviated by it. Emission and absorption processes are characterized as bound-bound, bound-free or free-free, depending on whether the electrons are in bound or free states before and after the transistion has taken place. In the solar atmosphere we can see examples of all three types of processes.

Bound-bound processes are processes where an electron in an atom or ion makes a transition from one orbital (the energy levels in the atom) to another. Either a photon is absorbed, moving an electron from a lower to a higher orbit, or an excited electron may make a downward transition to a lower orbit, emitting a photon in the process.

Bound-free (or free-bound) processes are processes where either a photon ionize an atom in an absorption-process (bound-free) or there is a spontaneous emission as an electron binds itself to an ion and thus releases energy in the form of a photon (free-bound).

Free-free radiation occurs when a particle (electron, ion or atom) is accelerated due to different situations such as collisions between particles (without any change in the particle's energy state), or external influence from magnetic or electric fields. When the particle is accelerated it will emit photons. Examples of free-free processes are bremsstrahlung, cyclotron radiation and Thompson scattering.

2.1.1 The Ca II H line

Calcium is an element with atom number 20 and two electrons in the outer shell. There are two resonance lines originating from singly ionized calcium, named the H and K lines. Resonance lines are lines occuring when a photon absorbed by the atom has the exact same energy as one of the excitation energies of the atom, thus sending out a photon of the same energy when deexcitation occurs. Since both photons have the same energy, an elastic scattering is the result.

The Ca II H line emits at 3968.5 Å. Calcium is singly ionised at 5000 to 20000 K, which puts these emissions in the chromosphere (see Figure 2.3 for a model of the temperature distribution in the solar atmosphere). At temperatures higher than 20000 K calcium is doubly ionised, and at temperatures lower than 5000 K we have recombination to Ca I.

The H line has most of its emission in the chromosphere and can thus be used to observe this region.

2.2 Radiative transfer in the solar atmosphere

How radiation is transferred through the solar atmosphere is an important part of understanding how the observed radiation and the state of the matter are the way they are. Radiative transfer techniques are important in both understanding the solar atmosphere and in modelling it. Radiative transfer

is used to explain where the radiation originates, and is thus applied for both the solar interior and the solar atmosphere.

2.2.1 Local thermodynamic equilibrium (LTE)

In a warm gas, thermodynamic equilibrium is defined to be when the gas is in thermal, mechanical and chemical equilibrium, i.e. the temperature is constant, the velocities of the particles follow a Maxwell-Boltzmann probability distribution and the concentration of the chemical components remain constant.

Local thermodynamic equilibrium can be assumed in systems where the system as a whole is not in thermodynamic equilibrium, but locally the changes are slow as opposed to the physical processes of interest, making it possible to use thermodynamic equilibrium as an approximation locally.

In the photosphere and solar interior, the high density makes it possible to simplify the theory, mainly by assuming LTE. In the chromosphere the density is considerably lower, yet the plasma is not completely transparent. Assuming LTE is no longer possible.

2.2.2 Radiative intensity and optical depth

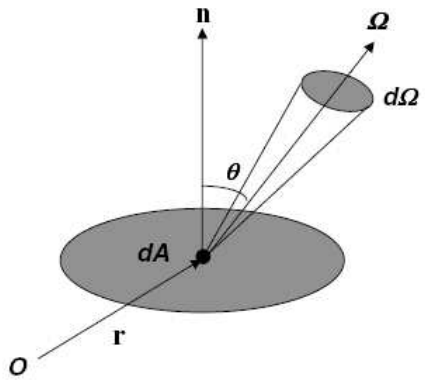

Figure 2.1: Radiative transfer through an area dA, travelling in a direction $\mathbf{\Omega}$, from Leung (2006)

The specific intensity I_ν is defined as the radiative energy per second for the frequency interval between ν and $\nu + \mathrm{d}\nu$ flowing through an area dA in the direction $\mathbf{\Omega}$ with $\mathbf{n}$ normal to dA during a time interval $(t, t + \mathrm{d}t)$ over the solid angle dΩ. Or:

$$\mathrm{d}E_\nu = I_\nu(\mathbf{\Omega}, \theta, t)\mathrm{d}A\cos\theta\mathrm{d}\Omega\mathrm{d}\nu\mathrm{d}t. \tag{2.1}$$

To convert this to wavelength, the relation $I_\nu = I_\lambda\frac{\lambda^2}{c}$ can be used. Locally, the radiation may be altered by absorption or emission when it passes

through a gas. Absorption removes photons from the beam, while emission adds to it.

The change in the monochromatic intensity, $\mathrm{d}I_\nu$, due to absorption as the radiation travels through a gas is given by

$$\mathrm{d}I_\nu = -\kappa_\nu \rho I_\nu \mathrm{d}s = \alpha_\nu I_\nu \mathrm{d}s. \tag{2.2}$$

Here, κ_ν is the opacity, ρ the density of the gas and $\mathrm{d}s$ the distance traveled by the radiation. α_ν is the monochromatic absorption coefficient, i.e. it measures how much the loss of intensity is due to intermittent absorption by dust or gas.

The change in monochromatic intensity due to emission is given by

$$\mathrm{d}I_\nu = j_\nu(s)\mathrm{d}s \tag{2.3}$$

where j_ν is the emissivity.

The optical path length (a measure of the distance a beam can travel through a medium before it is absorbed or scattered by the medium) is given by the following equation:

$$\mathrm{d}\tau_{\nu\mu} = \kappa_\nu \rho \mathrm{d}s = \alpha_\nu \mathrm{d}s. \tag{2.4}$$

Here $\mathrm{d}s$ is the distance measured along the beam's path in its direction of propagation. If we have a medium of thickness D, the optical thickness is $\tau_{\nu\mu}(D) = \int_0^D \alpha_\nu(s)\mathrm{d}s$. The medium is optically thin if $\tau_{\nu\mu}(D) < 1$ and optically thick if $\tau_\nu(D) > 1$.

So far the optical path length has only been described along the ray. We can define optical depth along the normal of the atmosphere in relation to the height, z, through (see Figure 2.2)

$$\mathrm{d}\tau_\nu = -\kappa_\nu \rho \mathrm{d}z = -\alpha_\nu \mathrm{d}z. \tag{2.5}$$

If the observer is observing at an angle θ to the radial direction, we get the relation

$$\mathrm{d}\tau_{\nu\mu} \equiv -\alpha_\nu \frac{\mathrm{d}z}{\mu} \tag{2.6}$$

where $\mu = \cos\theta$ and $\mathrm{d}z$ is the height in the radial direction. When $\theta = 0$ this is then reduced to $\mathrm{d}\tau_\nu$.

Looking at the Sun from its center and outwards towards its limb, it is possible to see that the relative brightness at the limb is less than at the center of the disk. This effect is known as *limb darkening*, and is due to the fact that we are not looking as deep into the atmosphere on the limb as we do at the disk center. Viewing the limb, the Sun is less dense, less thick and has a lower temperature, which means that the limb is less bright. Limb darkening is most prominent in visible light (the hot corona will make the limb bright at shorter wavelengths/higher energies, for example).

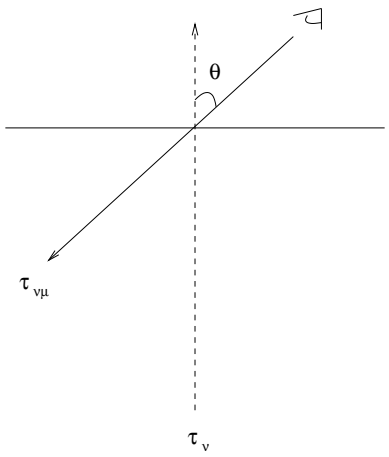

Figure 2.2: Optical depth in a plane-parallel atmosphere.

2.2.3 The source function

The radiation transport along a beam is given by

$$\mathrm{d}I_\nu(s) = I_\nu(s+\mathrm{d}s) - I_\nu(s) = j_\nu(s)\mathrm{d}s - \alpha_\nu(s)I_\nu(s)\mathrm{d}s \tag{2.7}$$

This is called the transport equation. The intensity along a beam does not change unless photons are added or subtracted from the beam. Rearranging this equation we get the change in intensity as the light propagates through the medium:

$$\frac{\mathrm{d}I_\nu}{\mathrm{d}s} = j_\nu - \alpha_\nu I_\nu \tag{2.8}$$

or

$$\frac{\mathrm{d}I_\nu}{\alpha_\nu \mathrm{d}s} = S_\nu - I_\nu(s) \tag{2.9}$$

where $S_\nu \equiv j_\nu/\alpha_\nu$ is the *source function*. The source function gives us the contribution the medium gives to the intensity due to absorption and emission. Substituting Equation 2.4 into this, leaves us with

$$\frac{\mathrm{d}I_\nu}{\mathrm{d}\tau_{\nu\mu}} = S_\nu - I_\nu(s) \tag{2.10}$$

i.e. the change in intensity with optical distance along the ray.

In LTE, the medium will radiate as a black body, and the source function is simply the temperature-dependent Planck function, $S_\nu = B_\nu(T)$.

Models of stellar atmospheres are often simplified by assuming a plane-parallel geometry, i.e. that the atmosphere is stratified with each layer having a constant source function. Another simplification is assuming that the

atmosphere is semi-infinite, so that the layers are parallel to each other. With plane-parallel geometry, the transport equation takes the form

$$\mu \frac{\mathrm{d}I_\nu}{\mathrm{d}\tau_\nu} = I_\nu - S_\nu. \tag{2.11}$$

For a semi-infinite stellar atmosphere, the emergent intensity ($\mu > 0$) is

$$I_\nu^+(\tau_\nu = 0, \mu) = \int_0^\infty S_\nu e^{\frac{-\tau_\nu}{\mu}} \frac{\mathrm{d}\tau_\nu}{\mu}. \tag{2.12}$$

The source function of spicules

In order to be able to say anything about the source function of the spicules, a few assumptions must be made.

Viewing spicules in the Ca II H line, it can be assumed that the medium is optically thin. Looking at one single spicule it can also be assumed that this is homogenous (constant density throughout the spicule) and that the width and depth are the same (i.e. that the spicule is cylinder-shaped).

The intensity emerging from the spicule will then be

$$I_\nu = S_\nu \cdot \Delta\tau_\nu = S_\nu \cdot \kappa_\nu \cdot \rho \cdot \Delta x \tag{2.13}$$

where $\Delta\tau_\nu$ is the optical depth, κ_ν is the opacity and Δx is the geometrical depth. This means that knowledge of the source function can tell us something about the density.

Unfortunately it is impossible to measure the source function observationally. The source function can only be determined with three dimensional computer simluations, which lie outside the scope of this thesis. However, some knowledge of the source function can be gained by comparing the scale heights of the density and the intensity. From Equation 2.13 it can be seen that if the source function is constant, then the scale height of the intensity will be equal to the scale height of the density. This will be explored further in Section 3.7.

2.2.4 Modelling the solar atmosphere

Since the solar atmosphere is a complicated system, we are dependent on computer simulations in order to understand the processes at work. The simulations are based on theories and are verified if the simulated "observations" look the same as real observations.

There are many different atmospheric models to choose from. One of the more well known ones is named the VAL3C model. The VAL3C model (Vernazza et al. (1981)) uses observations of the center of the solar disk in UV to radio to obtain the temperature-height relation from the deep photosphere to the transition region. It is simplified by assuming a plane-parallel geometry as well as hydrostatic equilibrium (i.e. the gravitational

pull downwards is balanced by the gas pressure gradient). The model is also in non-LTE (NLTE). The NLTE ionization and excitation equilibria for a number of atoms are solved simultaneously.

The average temperature distribution of the quiet Sun for the VAL3C model is plotted in Figure 2.3.

The height scale (x-axis in Figure 2.3) has its zero value at $\tau_{500} = 1$ and increases towards the left. The model gives us the approximate depths where different continua and emission lines originate (indicated in the figure). The figure shows how the temperature decreases from $h = 0$ (bottom of

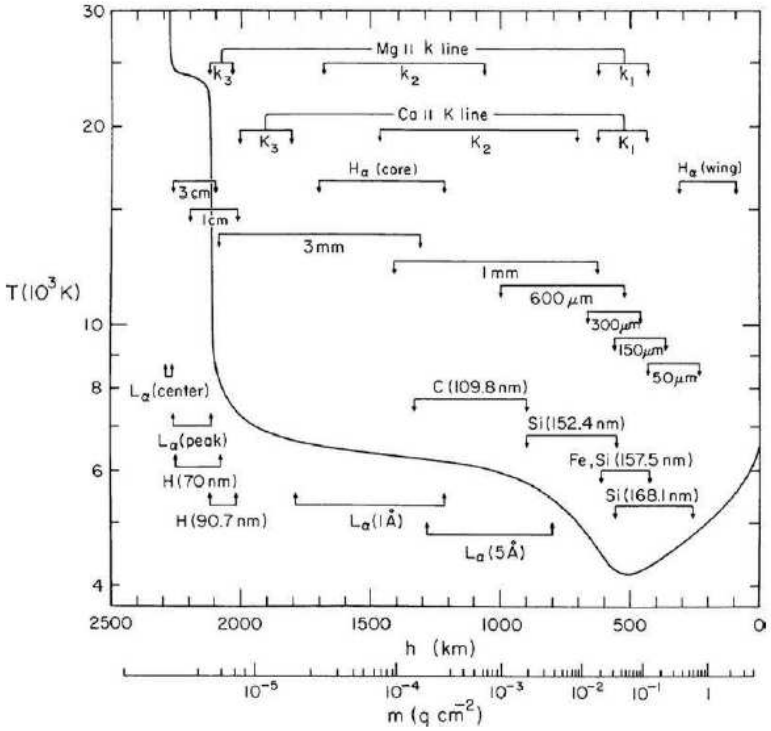

Figure 2.3: The average temperature distribution of the quiet Sun as modelled by Vernazza et al. (1981).

photosphere) out to $h = 500$ km. At this minimum the chromosphere starts by definition. The chromosphere reaches out to about $h = 2000$ km where there is a steep rise in temperature, known as the transition region. The figure also shows the formation heights of some important spectral lines.

The main problem with a model like this, is that it assumes hydrostatic equilibrium. Hydrostatic equilibrium is the state where compression due to gravity is balanced by the pressure gradient. Spicules, however, are seen to be much too dynamic and inhomogenous to be in hydrostatic equilibrium. For

the same reasons, a plane-parallel model may not be the best approximation either.

Chapter 3

Methods

> *If you want to make an apple pie from scratch, you must first create the universe.*
>
> –Carl Sagan

In this Chapter there is in Section 3.1 background information on the Hinode spacecraft, describing important aspects of its functions and optics.

In Section 3.2 there is a general description of CCDs and how they work, and some important information on the CCDs used to record the data used in this thesis.

In Section 3.3 the data reduction methods are described, while in Section 3.4 the process of searching for appropriate datasets is outlined.

In Sections 3.5-3.8 methods for calibrating the data and extracting useful information from the data are described.

3.1 Hinode

The Japanese Hinode (Japanese for "sunrise") spacecraft (formerly known as Solar-B) was successfully launched on 22 September, 2006. The mission is a collaboration between the space agencies of Japan (JAXA), United States (NASA) and Europe (ESA).

Hinode's scientific payload consists of three instruments: The Solar Optical Telescope (SOT), the EUV Imaging Spectrometre (EIS) and the X-ray Telescope (XRT). The three instruments together form a powerful tool for observing the Sun at many different wavelengths originating from the photosphere to the upper corona. They can work together, observing the same area at the same time, or seperately. The three main goals of the mission (Kosugi et al., 2007) are as follows:

- "To understand the processes of magnetic field generation and transport including the magnetic modulation of the Sun's luminosity."

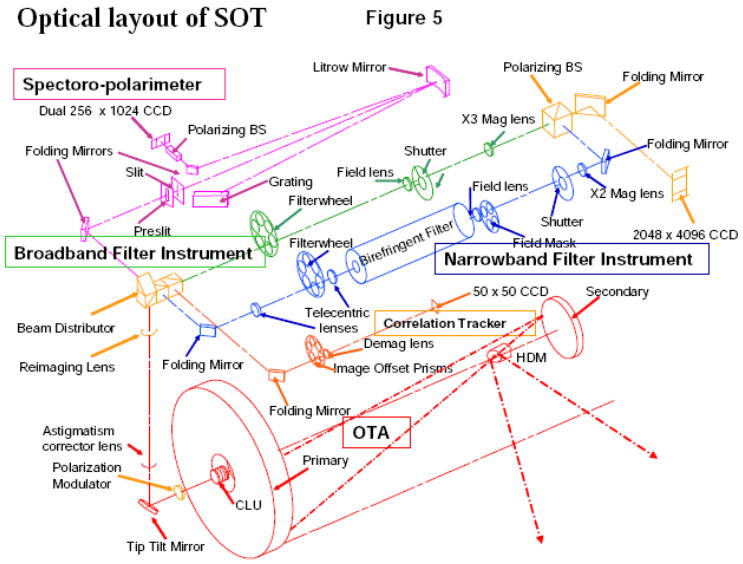

Figure 3.1: Optical layout of SOT (from Tsuneta et al. (2007)).

- "To investigate the processes responsible for energy transfer from the photosphere to the corona and for the heating and structuring of the chromosphere and the corona."

- "To determine the mechanisms responsible for eruptive phenomena, such as flares and coronal mass ejections, and understand these phenomena in the context of the space weather of the Sun - Earth System."

Hinode orbits in an elliptical polar orbit about 680 kilometers above the Earth's surface with a period of 98 minutes. Hinode can observe the Sun continuously for a duration of nine months each year. During the remaining three months, the spacecraft is regularly eclipsed by the Sun. This period of time is called the eclipse season and is described in more detail in Section 3.1.2. The spacecraft is controlled from the command centre at the Uchinora Space Centre in Japan.

3.1.1 Solar Optical Telescope (SOT)

The SOT is the largest solar optical telescope in space up to this date. It consists of an Optical Telescope Assembly (OTA) and a Focal Plane Package (FPP), (Tsuneta et al. (2007), Ichimoto and team (2007), Hurlburt et al. (2007)).

For full optical setup of the SOT see Figure 3.1.

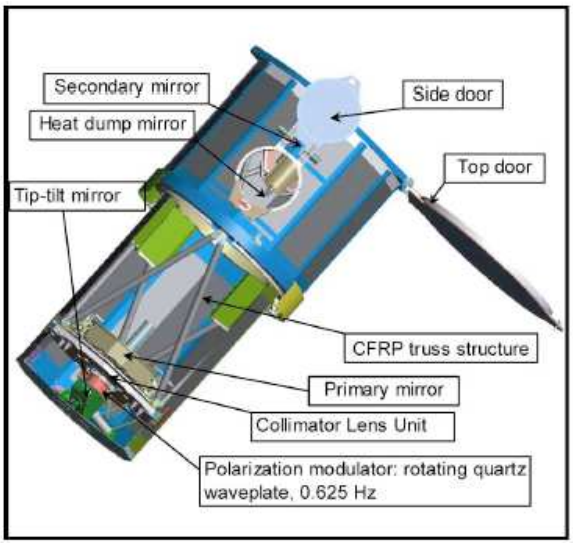

Figure 3.2: The SOT Optical Telescope Assembly (from Hurlburt et al. (2007)).

Optical Telescope Assembly (OTA)

The OTA (Figure 3.2) is a 50-cm aperture in an aplanatic Gregorian setup and is diffraction limited (0.″2 to 0.″3) between 3880 Å and 6700 Å. The OTA consists of the primary and secondary mirrors, a heat dump mirror, a Collimator Lens Unit (CLU), a Polarization Modulator Unit (PMU) and a tip-tilt mirror. The purpose of the heat dump mirror is to get rid of excess heat in the telescope, reflecting light out of the telescope through a sidedoor. The CLU collimates the incoming light so that the light is parallell before reaching the FPP. The PMU is a continuously rotating waveplate, with a period of 1.6 seconds, that provides polarization modulation.

Focal Plane Package (FPP)

The FPP has four optical paths: The Narrowband Filter Imager, the Broadband Filter Imager (BFI), the Spectro Polarimeter and the Correlation Tracker. In this thesis BFI datasets are used.

The BFI has interference filters for diffraction-limited imaging of the photosphere and lower chromosphere. The filter has a field of view of 218″ x109″ with 0.″053 per pixel, see Figure 3.3.

3.1.2 Eclipse season

During a part of each year the Hinode spacecraft enters a period where it is regularly eclipsed by the Earth (the Eart passes between the spacecraft and

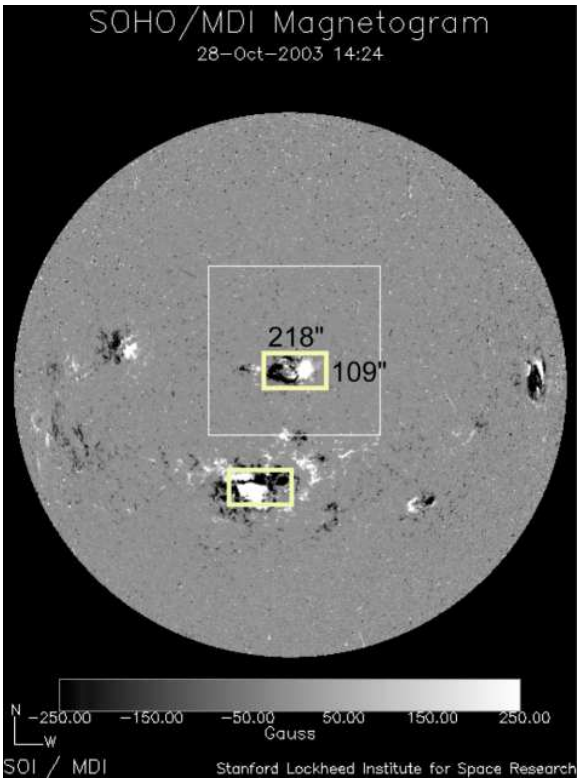

Figure 3.3: Field of view of the BFI superimposed on a SOHO/MDI magnetogram (from Hurlburt et al. (2007))

the Sun). Aside from giving fewer observations in this time period, it also affects the temperature aboard the spacecraft as it is no longer constantly exposed to the heat of the solar radiation. This may then affect the observations. In Figure 3.4 the duration of the eclipses of 2007 is plotted as a function of time. The eclipse season in 2007 lasted from the 5th of June to the 3rd of August. In analyses, where variations over time is investigated, the eclipse season and its effect on the instrument should be investigated and taken into account.

3.1.3 Filters

SOT can perform observations with both a filtergraph, i.e. images where the light is filtered so only light of a specific wavelength (or range around a wavelength) is let through, and a spectrograph, i.e. obtaining images of the spectrum. SOT has two filter imagers, one broadband (BFI) and one narrowband (NFI). In this thesis only the BFI was used.

The BFI uses interference filters to image the CN and CH ("G-band")

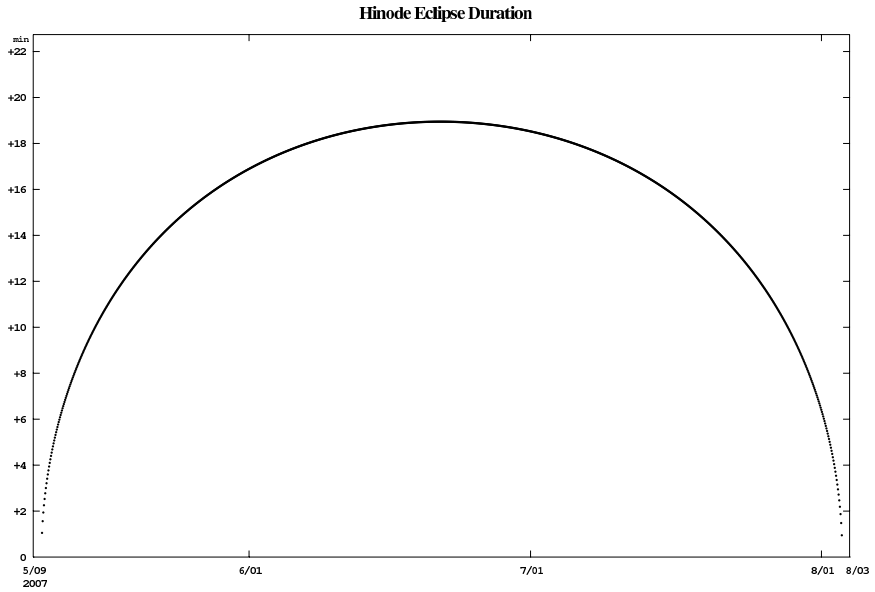

Figure 3.4: The duration of the eclipses in minutes as a function of time for the 2007 eclipse season[1].

lines in the photosphere, the Ca II H line for the lower chromosphere and also blue, green and red continuum measurements. In this thesis mainly the Ca II H line filter (396.85 nm) was used, while observations in blue continuum and G-band were used for calibrations. The BFI centered on the Ca II H line has a bandwidth of 0.8 nm, and has an almost Gaussian shape with a FWHM[2] of 0.22 nm (Carlsson et al. (2007)). This is broad enough to allow emission from both the chromosphere and the photosphere to pass through.

In Figure 3.5 the transmission filter profile for the Ca II H line has been plotted against a solar spectrum (taken from the Sac Peak atlas from 1976 made by Beckers, Bridges and Gilliam). The plot was made with an IDL routine from the Hinode tree of solarsoft, `fg_bfi_filter.pro`. It shows the transmission (i.e. the amount of light that the filter lets through) of the BFI interference filter (the black line) as a percentage of the solar flux (purple line). In the center of the line the transmission is approximately 65%.

The transmission was measured on the ground before launch of the spacecraft. The sensitivity of the telescope as a whole (including its filters) very likely changes with time. A test on this is described in Section 4.3.2.

In order to test whether the BFI is actually suitable for studying chromospheric dynamics, Carlsson et al. (2007) determined the intensity response function to perturbations in the temperature.

A response function (Magain (1986)) measures the response of a quan-

[2]Full Width at Half Maximum

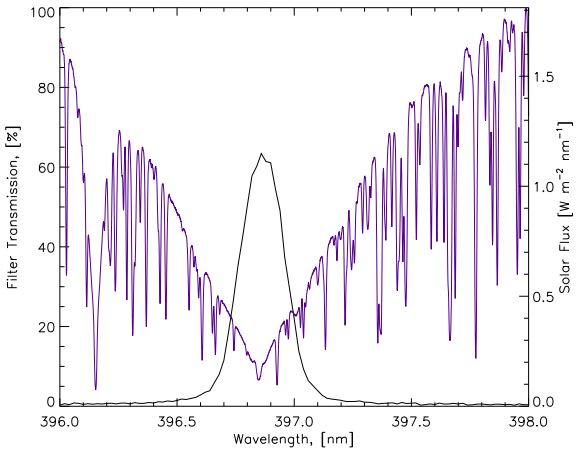

Figure 3.5: Filter transmission for the Ca II H line.

tity to a given perturbation. Carlsson et al. (2007) measured the response function of the relative change in intensity, given a perturbation in the temperature, as a function of height in the atmosphere. The response function was calculated numerically for a six level model atom of Ca II with the simulation software MULTI (Carlsson (1986)). The resulting intensity profile was then multiplied with the BFI filter transmission profile and integrated. Though the method has its flaws, the result can give an indication of from where intensity variations originate in the atmosphere. The response function for Ca II H can be seen in Figure 3.6 (*solid line*), along with those of blue continuum (*dashed line*) and G-band (*dashed-dotted line*).

From this figure it can be seen that the Ca II H filter samples a wide region in the atmosphere, with a mean response height at 247 km. The long tail of the Ca II H response function stretches well into the middle chromosphere, showing that the Ca II H line is observable in the lower to middle chromosphere with the BFI.

3.1.4 Data processing

Onboard the spacecraft, the Mission Data Processor (MDP) governs the three scientific instruments. In addition to regular observations the three instruments can switch over to observe flares if the system detects an outbreak of flares. The MDP also controls the observations and data recording. The MDP compresses the data two times for faster data downloading to Earth: First pixel-by-pixel and then image compression. The image compression can be either lossless (by Differential Pulse Mode Modulation - DPCM) or lossy (Joint Photographic Experts Group - JPEG). Finally the image gets

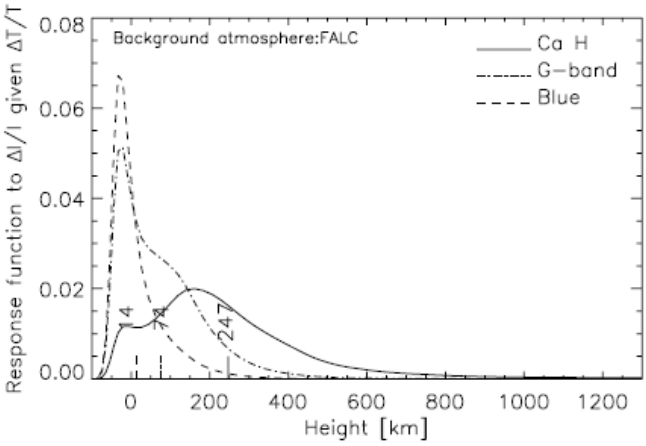

Figure 3.6: Response functions for the BFI filters (from Carlsson et al. (2007)). The solid line is the Ca II H line, the dashed line is blue continuum and the dashed-dotted line is G-band.

stored in the data recorder, waiting to be downlinked. It is highly necessary to consider onboard image compression during preparations for observations, due to the satellite's limited contact with the ground stations. A flow chart of the steps of data aquiring and processing can be seen in Figure 3.7.

The data are downlinked to several stations, including Uchinoura Space Centre station and the Norwegian ground station at Svalbard, reformatted into FITS[3] files and made available to the scientific community. The data was initially downloaded 15 times each day at Svalbard, with a total of approximately 42.5 Gbits of data per day, but the number of downlink stations have later been increased, resulting in 40 downlinks each day.

Since December 2007 there have been problems with the primary antenna aboard the space craft transmitting in the X-band (4 Mbps), making it necessary to switch to the secondary antenna transmitting in the S-band (32 kbps). This has limited the potential for the amount of data that can be downloaded, which is reflected in the data used in this thesis.

The data used in this thesis is freely available, and is not part of observations planned for this thesis. A thourough search through the data archive was then necessary in order to find appropriate datasets (see Section 3.4).

[3]Flexible Image Transport System - a digital file format commonly used for images in astronomy.

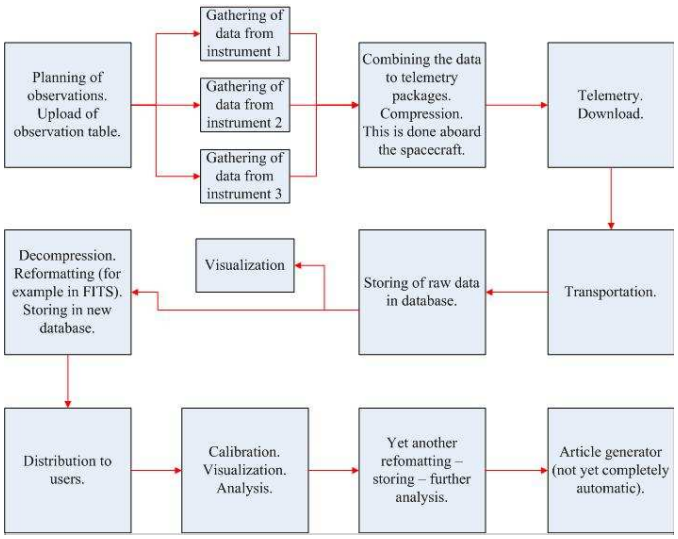

Figure 3.7: Schematic drawing of the recording and processing of data (copied from Øivind Wikstøl (2006))

3.2 Charge-Coupled-Devices (CCDs)

Charge-Coupled-Devices (CCDs, see e.g. Howell (2000)) are the detectors used to record data in the optical part of the spectrum, replacing the old method of using photographic plates and film. CCDs were first used for astronomical observation in 1975, and has since become the most important means to record astronomical data. Simply put, the number of incoming photons is changed into a digital number which then can be interpreted as an image on a computer. They are used for four main methods in astronomy: imaging, astrometry, photometry and spectroscopy. CCDs are made of silicon, which makes them very sensitive to optical wavelengths (3000 to 10000 Å), and their sizes are measured in pixels ("picture elements"). Each pixel is electronically isolated from the others, and thus measures the incoming photons only in that small area which it spans. CCDs have the advantage of having very low internal noise production in addition to having a high quantum efficiency (QE) and good bandpass, as opposed to other detectors available. Modern CCDs have a noise level of only a few up to fifteen electrons per pixel.

The QE is a measure of how good the detector is at converting incoming photons to useful output, and is defined as the ratio between the number of incoming photons to the number of detected photons. Photoelectric plates have a QE of around only 2 %, while modern CCDs can boast a QE peak of 90 %, and at least 60 % over two thirds of the total spectral range.

3.2.1 Detection and read-out

The workings of a CCD is based on the manipulation of electrons produced in the CCD when it is exposed to light. The produced photoelectrons are stored by means of a metal insulator semiconductor (MIS) capacitor. The CCD itself is made up of many of these capacitors. In addition, voltages are used to move the charges around. The production of electrons in the CCD is due to the photoelectric effect. Incoming photons hit the silicon in a pixel and are absorbed (as long as they have the right energy). The silicon then releases a valence electron which is transferred into the conduction band. Outside of the spectral range of the silicon, the material is completely transparent for the incoming radiation. On each pixel, voltages called "gates" are placed to keep the silicon from re-absorbing the released electrons. In the most common setup, each pixel has three gates capable of having different voltages (the middle one with higher voltage than the two on each side of it), thus creating voltage wells to trap the electrons in. When the exposure is done, the voltages of the gates are changed systematically so that the electrons collected are moved out of the pixel arrays and into an output register. The output register is in reality just another row of pixels which have not been exposed to the light. In the output register, each pixel charge is amplified by an output amplifier and then read out and converted to a digital number (often called counts or analog-to-digital units (ADU)). The size of the arrays in a CCD is limited by the manufacturing processes: First by how large an electrical circuit can be made and still be of good quality, and second by how small the MIS capacitors can be made.

3.2.2 The CCDs of the BFI

The BFI aboard Hinode shares its CCDs with the NFI. There are two CCDs coupled together to function as one, with a size of 4096x2048 (4K $\times$ 2K) pixels. This gives a maximum field of view of $218'' \times 109''$ and a resolution of $0\overset{''}{.}054$ per pixel.

Summing

It is possible for the observer to turn on *summing* (also called *binning*) when observing to make better use of the downlink time. Summing is when the onboard computer sums the pixels in either a 2×2 or 4×4 configuration. Instead of getting one (data) number per pixel, we then get one number per either four pixels or sixteen pixels, which is a clear advantage when dealing with the restrictions in the amount of data possible to download to Earth. The read-out time for the full CCD is 3.4 seconds for 1×1 summing, 1.7 seconds for 2×2 summing and 0.9 seconds for 4×4 summing, giving further advantage if the observer wants to take exposures with a minimum amount of time in between.

This solution may mean poorer resolution, depending on the wavelength imaged. For the Ca II H line it is possible to do a 2×2 summing with minimal effect on the resolution, while 4×4 summing will have such a large effect that it is not used. It is not a major problem with 2×2 summed images for the work done in this thesis, but use of summed images is avoided when possible.

3.3 Data reduction

There is always some data reduction needed when dealing with astronomical data. There may be known flaws in the instruments which can be removed, or known optical aberrations. The Hinode data is no exception to this. In this Section, the data reductions done to the data will be explained.

3.3.1 IDL and SolarSoft

Interactive Data Language (IDL) is an array-oriented data analysis and visualization programming environment (see e.g. Gumley (2002)). It is the main programming environment used for analysis of Hinode data. The Hinode team has developed a series of IDL-packages available as a part of the SolarSoft system.

The SolarSoft system is a set of software libraries, databases and system utilities created to be applicable to solar physics. The SolarSoftWare (SSW) is built up by software libraries from several space-borne telescopes as well as general astronomy software. The SSW is primarily based on IDL but in some cases other programming languages may be integrated into the routines. In this thesis both SSW routines and routines written by my supervisor Mats Carlsson or myself have been used.

3.3.2 First round of image corrections

Hinode analysis software is released as a part of SolarSoft by the Hinode team. This software includes the routine `fg_prep.pro`, which corrects the images for *dark current* and *flat fielding* among other things.

Dark current

Unfortunately, photons are not the only source of photoelectric charge generated in the CCD. There are always some electrons moving around due to natural thermal movements, and are thus causing a current which is called dark current (since it is not due to any light actually hitting the CCD). Dark current is then highly dependent on temperature, and the only way to reduce the error caused by it is to lower the operating temperature. It is also strongly dependent on the fabrication process and the quality of the

silicon used to produce the CCD. The routine `fg_prep.pro` includes a model of how dark current varies with the temperature on the CCDs in the FPP and removes the dark current signal from the images.

Flat fielding

There are always small differences from pixel to pixel in the CCD. They can for example have different gain[4] and quantum efficiency (QE).[5] To remove these effects from the images, a flat-field image is used. The ideal flat-field image would be one where there has been a uniform (known) illumination of every pixel in order to obtain information about the variations from pixel to pixel. This should preferrably be done with a light source with similar energy distribution to that of the object images.

For the Ca II H-line in the chromosphere, it is difficult to obtain a flat-field image due to all the dynamic variations in the image. For it to be done successfully, a lot of images are needed that can be combined into a mean image with very little variations. In most of the data used for this thesis, the `fg_prep.pro`-routine uses a CN-flatfield (3883 Å), but in early 2008 a Ca II H-flatfield was also added to the SolarSoft/Hinode-tree. However, the difference between the two flatfields on Ca II H-data is negligible, and the data corrected before 2008 have not been processed again due to this.

Read-out error correction

The SOT camera consists of two CCDs in which the last column in the first CCD and the first column in the second CCD are empty of data. An interpolation over these two columns is done in `fg_prep.pro` to compensate for this.

South Atlantic anomaly and cosmic radiation

Hinode passes through the South Atlantic anomaly (a region of strong radiation due to the inner van Allen radiation belt in the Earth's magnetosphere). When these high-energy particles hit the instruments aboard the spacecraft, they induce static interference in the images, seen as white dots crossing the field of view. Due to their fast movement and relatively short appearance in the image series it is assumed that it does not effect the calculations done with the intensity to any notable degree (and thus not important enough to be removed in the datasets used in this thesis).

In addition to the South Atlantic anomaly, there is also the possibility of interference for high energetic cosmic radiation. It is possible to correct for this interference with `fg_prep.pro`, but it is not turned on by default

[4]Gain: Number of electrons needed to produce one ADU (analog-to-digital unit)

[5]The QE is the efficiency of the CCD and is given by the ratio of the number of absorbed photons to the number of incoming photons

and has not been used in the data for this thesis (mainly because this part of the routine was not finished before it had been used for most of the datasets). It is assumed that these interferences have a negligible effect on the measurements.

3.4 Datasets

Appropriate datasets were found by using the search webpage for the Hinode Science Data Centre Europe[6] and then copied for use with the help of IDL. Each search is accompanied by a small IDL-code that retrieves the paths to the data files (assuming they are on a local network hard drive; it is also possible to download the files from the website).

A dataset, or image series, is a set of images taken with the same program, i.e. with the same observational criteria (such as FoV, exposure time and so on). The only things that change between each image is the time at which it was taken, and in some cases the filter with which it was taken.

There were several criteria used as a basis for finding appropriate datasets:

- Time series of at least 400 images to get a long enough time span for studying the variations and life span of spicules.
- Cadence[7] of less than 14.4[8] seconds in order to get high enough time resolution for observing spicules.

In the time period from November 2006 to December 2007, 234 time series were found to satisfy these requirements (see Appendix B). Additional criteria used if possible were:

- Preferably long exposure times (≥ 0.5 s).
- Preferably not summed datasets.
- Preferably a large field of view (FoV).[9]

To observe spicules, one must use images of the limb since spicules on the disk have yet to be conclusively identified.

3.4.1 Cubes

The image series are combined into data-cubes (basically a three dimensional array) that makes it easier to view them as a movie. The process of combining the SOT FITS-files into data-cubes includes using `fg_prep.pro` to do the

[6] `http://sdc.uio.no/sdc/`
[7] I.e. time span between each exposure
[8] Nine times the 1.6 rotating period of the Polarization Modulator (PMU)
[9] Maximum FoV is 4096x2048 pixels (2048x1024 for summed images).

image reduction as described above. In addition, the header information is stored away in its own file. Each image has its own header information. The header information contains a lot of information about the files such as observing time, exposure time, field-of-view etc.

3.5 Aligning the images

Aboard Hinode, there is a correlation tracker which locks on to structures on the disk and tries to compensate for most of the jitter caused by the spacecraft. The correlation tracker locks on to structures on the disk, and keeps those structures at the same place in the FoV throughout the time series. This removes most of the jitter and is also useful when viewing structures on the disk, since they will be in the same place through the whole dataset. However, as the Sun rotates, and the surface structures with it, the correlation tracker moves with them. This causes the limb to drift across the FoV, which is *not* an advantage when viewing structures off the limb. Instead it is of interest to keep the limb in the same position throughout the time series.

To correct this drift, routines were used that identify the limb and keep it in one place throughout the image series, through cross-correlation from image to image. This is done by first calculating the shift between each image and then correcting for this shift and storing the result in its own data cube.

3.5.1 Calibration of the limb

It is of interest to calibrate the limb of a certain line relative to $\tau_{500} = 1$ (the height where the monochromatic optical depth equals one, for light emitted at 500 nm), since this is used in much of the literature as the zero point for the height scale in the solar atmosphere. It can then be used as an absolute scale for the limb and other observables. Hinode/SOT can observe in what is called the blue continuum, centered around the wavelength of 4504 Å (blue light). Using a VAL3C-model and the MULTI software (Carlsson (1986)) for modelling the solar atmosphere, the height difference between $\tau_{500} = 1$ and the limb at 4504 Å can be found.

MULTI is a computer program that can solve multi-level non-LTE radiative transfer problems. The program takes as input for example a model of the solar atmosphere at one specific wavelength. The calculation of the limb in MULTI is highly dependent on the model. For photospheric wavelengths, such as blue continuum, the differences between different models are relatively small, while at chromospheric wavelengths there can be large differences in where the limb is located. It is then better to find the blue continuum limb relativ to $\tau_{500} = 1$ with a computer model and then calculate

the difference between the blue continuum and calcium limbs observationally, rather than trying to find the calcium limb with a computer model.

Offset between wavelengths

The optics in the SOT refract the incoming light, making various wavelengths hit the detector at slightly different points. This offset between different wavelengths is known[10], and is easily corrected in the images. The images can then be compared with BFI images of other wavelengths to determine the difference in the height of the limb. The G-band values for the central pixel of the detector (2047.5, 1023.5) are used as zero values to which the other (five) filter values are compared. (See table A.1 in Appendix A).

Calculating the difference in limb height

After having corrected the images for the offset due to the optics in the telescope, the remaining difference between the Ca II H limb and the blue continuum limb is calculated in the following manner: First the x and y coordinates for the solar centre in calcium are found using a least-square fitting to the limb and assuming the solar disk to be a perfect circle. The limb is set to where the intensity scale height has its minimum, and is calculated for each row of pixels across the limb. Secondly, the limb is calculated for the blue continuum, but using the x and y coordinates for solar disk center found for calsium. The x and y coordinates are somewhat uncertain, due to limited curvature of the limb across the field of view, which makes it difficult to calculate them. But the scale of the x and y coordinates are accurate, making it possible to calculate the relative difference in height between the Ca II H limb and the blue continuum limb.

It is necessary to use images with as identical pointing (high cadence) as possible in order to reduce uncertainties from rotation of the Sun (causing the drift described above). Assuming that the image series have identical pointing, the only source of uncertainty is jitter from the spacecraft between the exposures.

3.6 Calibration of intensity counts

The intensity measured in the data is basically the counts (number of electrons knocked free by the incoming photons) taken by each pixel on the CCD. It is convenient to convert these counts into more normal units, such as cgs (ergs/cm^2/s/sr/Hz) or SI (J/m^2/s/sr/Hz) units, but this is not necessarily straightforward. Several factors influence the counts. First, there is the activity on the Sun which can vary greatly (with variations in the

[10] `http://solar-b.nao.ac.jp/hinode_wiki/index.php?FG%20pixel%20offset%20and%20scalesee`

emergent intensity as a result) from one dataset to another. Second, there is the exposure time. The counts in the images are all the incoming radiation from each exposure, which varies from dataset to dataset and sometimes even from image to image in the same dataset. Calculating counts per second is then easily done by taking the counts and dividing with the exposure time. Third, there are two factors due to the CCD, namely its quantum efficiency and data number per photon. There may also be other unknown factors in the telescope that affects the measured intensity. Fourth, there is the filter transmission as a function of frequency (see Section 3.1.3). Last, there is the overall reflectivity of the mirrors and the transmission through the lenses/windows in the optical setup, both of which are declining with time. Combining these factors we get the following:

$$N = a \cdot f(t) \cdot \mathrm{QE} \cdot \mathrm{d}\Omega \cdot \frac{1}{h\nu_0} \cdot \mathrm{A} \cdot S \cdot \mathrm{D} \int I_\nu \Phi(\nu) \mathrm{d}\nu \tag{3.1}$$

where N is the counts per (summed) pixel per second, a is the efficiency factor of the telescope for the total system, $f(t)$ is the time-dependent part of the total efficiency factor (which equals unity at $t = t_0$), QE is the quantum efficiency of the CCD, $\mathrm{d}\Omega$ is the solid angle of the telescope as seen from the Sun, $h\nu_0$ is the energy per photon (the wavelength range of the filter transmission is small enough that it can be assumed that all the photons have the same energy), A is the area of one pixel on the Sun, S is the summation factor (equals 1 for non-summed data and 4 for 2×2 pixel summing), D is the data-number of the CCD per photon, I_ν is the intensity from the Sun before passing through the telescope and $\Phi(\nu)$ is the filter transmission. Combining the time-independent factors into one, we get:

$$N = b \cdot f(t) \cdot S \int I_\nu \Phi(\nu) \mathrm{d}\nu \tag{3.2}$$

where $b = a \cdot \mathrm{QE} \cdot \mathrm{d}\Omega \cdot \frac{1}{h\nu_0} \cdot \mathrm{A} \cdot \mathrm{D}$.

We can determine the constant b if we use observations where we know I_ν, for example the average quiet Sun from a solar atlas (Brault and Neckel (1987)). The solar atlas gives the intensity only relative to the continuum intensity (that is not given), which means we also need a value for the continuum intensity. This was derived from a computer model, using the MULTI software (Carlsson (1986)) combined with the FALC model of the solar atmosphere (Fontenla et al. (1990)). The FALC is a semi-empirical model of the quiet Sun.

The filter transmission is known by the `fg_bfi_filter.pro`-routine (Section 3.1.3). The time-dependent efficiency factor, $f(t)$, can be found by looking at how the mean intensity in quiet Sun changes with time. This process will be described in detail in Section 4.3.2.

When all these factors are known, $\int I_\nu \Phi(\nu) \mathrm{d}\nu$ can be calculated from an observed N.

3.7 Intensity scale height

In order to see how the intensity varies with height in the atmosphere, using the scale height of the intensity can be very useful. The scale height of a variable is defined as the distance that it takes for the variable to decline by a factor of e. For the intensity, we have:

$$I(z) = I(z=0)e^{-\frac{z}{H(z)}} \tag{3.3}$$

$$\ln I(z) = \ln I(z=0) - \frac{1}{H(z)}z \tag{3.4}$$

$$H(z) = -\frac{1}{\frac{\mathrm{d}}{\mathrm{d}z}(\ln I(z))} \tag{3.5}$$

where $H(z)$ is the scale height, z is the height and $I(z=0)$ is the intensity at $z = 0$.

As intensity any observable proportional to the intensity can be used (for example the count given by the CCD which is dependent on the exposure time), since the proportionality constant will be multiplied on both sides of Equation 3.3.

The height z is an arbitrarily chosen height scale. It is of interest, though, to measure the height in relation to the much used $\tau_{500} = 1$ height, that is where the optical depth in 500 nm is equal to one, as discussed in Section 3.5.1.

3.8 Measuring spicules with xt-plots

In order to measure properties of spicules such as their velocities, decelerations, lengths and lifetimes, *xt-plots* are a powerful tool. In xt-plots, one slit (one pixel wide) along a chosen spicule is plotted with respect to the time. If there is movement along the slit in time this should be visible in the xt-plot as a curve at an angle with the x-axis (visible above the "non-moving" background consisting of lines parallel to the x-axis).

If a spicule appears as a linear line in the xt-plot, the velocity of the spicule is constant, while if it is curved it has an acceleration/deceleration. The larger the angle a linear spicule has with the x-axis, the smaller is its velocity. A spicule appearing as perpendicular to the x-axis in the xt-plot would have zero velocity, while a spicule parallel to the x-axis has infinite velocity.

Chapter 4

Results

> *And there never was an apple, in Adam's opinion, that wasn't worth the trouble you got into for eating it.*
>
> –Neil Gaiman

In this chapter the results obtained with the methods described in Chapter 3 will be presented and discussed.

The layout is as follows: First the process of selecting datasets is described. Finding good and useful datasets is a non-trivial task, and together with the basic data reductions this process took considerable time. This process is described in Section 4.1.

The dynamical nature of the spicules is difficult to present with single images and graphs. The visual impression that remains after spending much time studying movies is therefore described in Section 4.2.

It is always useful to give heights relative to some standard scale. In the field of solar atmospheric physics, the standard primarily used is height relative to $\tau_{500} = 1$ (where the optical depth at 500 nm is unity). The natural point of reference for the observations done in this thesis is the limb in calcium. Calibrating the height of the limb in calcium relative to the standard height is done in Section 4.3 and is an important result in itself.

As for the height scale, it is also of interest to calibrate the intensity scale. The intensity in the images from SOT is given in counts, while it is better to have the intensity in more useful units. The calibration process and results are given in Section 4.4.

Intensity scale heights are a useful tool for looking at how the intensity varies with height. More on this in Section 4.5.

The different characteristics of spicules (such as height, lifespans, velocities etc) can give valuable information about the driving mechanisms behind them. In Section 4.6 measurements of different characteristics for the two types of spicule populations are presented and discussed.

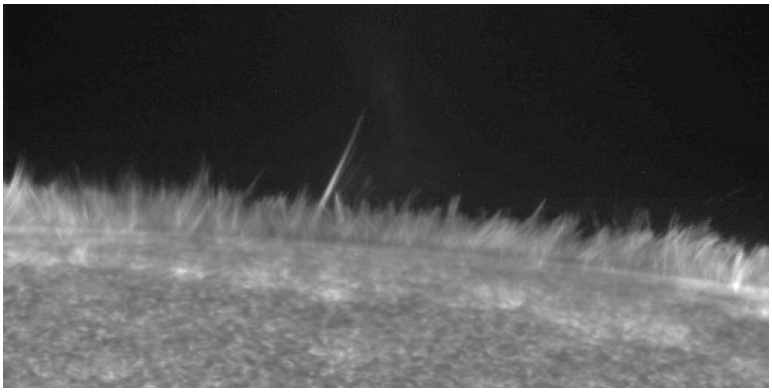

Figure 4.1: Spicules at the western equator.

4.1 Datasets

A complete table of the datasets on which the basic data reductions were done is given in Appendix B. This table includes both time series taken of the limb and of the disk. They have all been subjected to the initial round of data reduction with the `fg_prep.pro`-routine, and organized into data-cubes, before being scrutinized for further selection.

The header information accompanying each image includes information on the date and time the image was taken, the size of the Field of View (FoV) in pixels in the x and y directions, whether or not the data is summed, the exposure time, whether or not the correlation tracker was switched on at the time and where the FoV is in respect to the solar center.

With this information combined with the number of images in a time series, it is easy to calculate the cadence, the total time span of the time series and the cosine of the angle between of the line of sight and the radial direction, μ.

Finding the usable datasets was then a matter of exluding the poor ones. First to be excluded were all the datasets with images on the disk. There were also some taken on the limb where the amount of atmosphere visible was too small to be of any use. Since spicules are best viewed in the quiet Sun, datasets with sunspots and other types of active regions were also excluded.

The routines used for aligning the limb (described in Section 3.5) do not work with datasets were the limb is diagonal across the FoV instead of being more or less parallel to either the x- or the y-axis. This also exludes its share

of datasets. There are also some datasets where the align routines have not managed to compensate enough for the jitter from the spacecraft, possibly due to the correlation tracker not being turned on, or just because there is too much activity for the CT and routines to work properly.

After going through the 234 datasets and sorting out the ones that do not fulfill the criteria and needs, around 15 datasets remain from which to gain some important results.

4.1.1 Aligning

The align routines are optimized to compensate for the drift of the limb due to the correlation tracker having locked on to disk structures. They mainly compensate for the drift in the rotational direction. If the images are taken at the equator the drift is usually more pronounced than at the poles since the rate of rotation is faster at the equator and decreases as the latitude increases (differential rotation). The drift at the poles is observed to be perpendicular to the limb as well even though the rotation of the Sun is more parallel to the limb, if it can be said to exist at all at the poles. The reason for why this is, is unknown. If the correlation tracker is not turned on, the jitter of the telescope becomes too violent for the routines to be able to compensate for it in most cases.

All the images of a time series are corrected in relation to the first image of the series, along the x-axis for images of the equatorial limb and along the y-axis for images of the polar limb. If an image is shifted in one direction this will delete rows of pixels in one of the ends and introduce new rows in the other. In the new rows an interpolation is made. Since the limb usually crosses the FoV along or close to its middle, this does not affect the measurements done of the chromosphere, either because the interpolated rows are on the disk or too far out in the atmosphere to be included in the measurements.

For image series taken on the disk (and not the limb), the align routines do a cross-correlation from image to image, which depends on the routines being able to identify the same structures from image to image. If the time lapse between images are too large, or for example the images alternate between different filters, the routines may run into trouble.

4.1.2 Coronal holes

It is of interest to know whether or not coronal holes were present at the time the images were recorded to see if the spicules' properties differ between areas with coronal holes and those without.

Looking at images taken by the Extreme ultraviolet Imaging Telescope (EIT) aboard the SOHO spacecraft[1] (Figure 4.2) it is possible to see that

[1] `http://www.SolarMonitor.org/`

Figure 4.2: Image of the Sun taken with SOHO/EIT at 195 Å. (Courtesy of ESA/NASA.)

during the time since first light of Hinode, the appearance of coronal holes have been few and far between, in addition to those few being very small. They also all appeared either a little below or above the equator, making them avoid the datasets where the images are centered on the equator. With the available images from EIT (taken at 195 Å and 171 Å), no low-latitude coronal holes were found that coincided with the datasets used. However, the images are not always updated daily, and in addition the EIT is sometimes taken offline for 2-3 weeks due to a problem with the CCD that requires it to be heated up ("bakeout") in order to maintain its performance. Bakeouts are usually scheduled during periods when data loss aboard SOHO is expected anyway, for example due to periods with limited contact with Earth. Coronal holes may thus have slipped by undetected, though looking at the frequency and sizes of the observed coronal holes, it can be assumed that there were no coronal holes affecting the low-latitude datasets.

Since the images taken with SOHO/EIT is centered on the equator, it is not possible to see the whole of the polar regions. Looking through the available images, it is however possible to see coronal holes most of the time

in the parts of the polar regions that are visible. It is assumed then that at the images where there are no clear coronal holes visible, they are simply too small to be seen at the steep angle we are viewing the polar regions at, and that there are coronal holes at the poles constantly. In Figure 4.2 it can be seen that there are slightly darker regions at the poles. A weak, extended coronal hole can also be seen slightly to the right of the solar center.

It then boils down to the easy separation of the datasets into those taken at the poles, coinciding with coronal holes, and those taken at the equator, coinciding with "normal" corona.

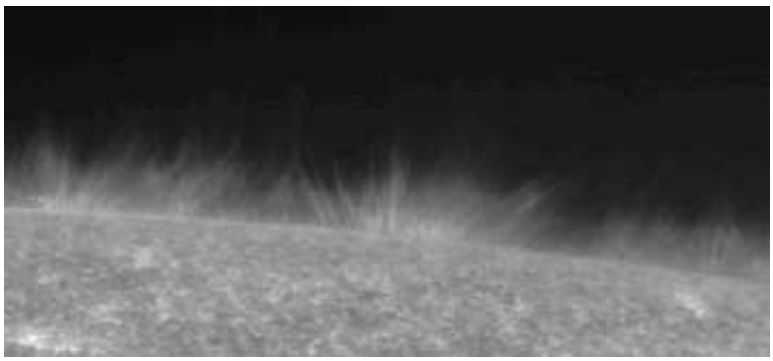

Figure 4.3: Example of rosetta structures.

4.2 Limb calibration

In calibrating the limb relative to $\tau_{500} = 1$ several steps are made, as described in the following subsections.

4.2.1 Optical offset

Correcting for the optical offset between the filters (table A.1), is just a simple matter of shifting pixel coordinates in the image accordingly with the built-in IDL routine `poly_2d` which performs a polynomial warping of the image.

To check whether or not the offset changes over time, the align-routines (Section 3.5) were used on a time series spanning the period from November 12th 2006 to December 2nd 2007, sampling around 180 days. All the images in the time series were from the synoptic program. This program is run every day and takes images with identical specifications for all filters, making it easy to compare images of different filters as well as investigating how they change with time. G-band and blue continuum were compared to each other since the align-routines' cross-correlation have problems correlating between

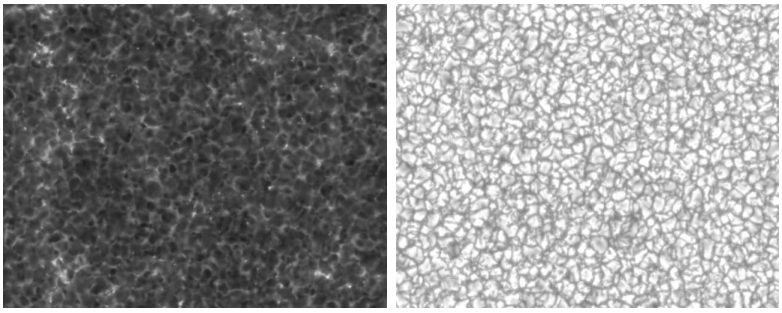

(a) (b)

Figure 4.4: Comparison of exposures of calcium (*left*) and blue continuum (*right*). It can be seen that the two different filters have inverse brightness.

calcium and G-band/blue continuum. This is because the brightness in the images are reversed for calcium relative to G-band/blue continuum, (see Figure 4.4), making it difficult for the align routines to correlate properly. Also the calcium emission originates from a greater height in the atmosphere, and the structures we see further down do not necessarily propagate straight upwards. Comparison between G-band and blue continuum will not have this problem, since they originate at the same height, see Figure 3.6. It is thus assumed that any trend that causes the offset to change with time will not be due to the filters changing, but have other origins in the telescope. Looking at the offset between G-band and blue continuum will be sufficient to determine whether or not the offset changes with time. This was done by sampling 182 pairs of images from the timespan 2006-11-12 to 2007-12-02. The result can be seen in figure 4.5.

The panels in this figure is the x- and y-direction respectively of the shift. Each data point corresponds to a pair of images, taken with less than a minute's time difference. Ignoring the outliers it is quite clear from these plots that the shifts do *not* change significantly over time.

It is, however, easily seen from the plots that there is a small variation in the shifts. The differences within one coordinate are most likely due to jitter in the telescope. Despite attempting to find image series where the exposures are taken as close to each other in time as possible, one cannot avoid the jitter completely. In addition, the correlation tracker was not switched on for most of the exposures. There is also the chance that the table with offset corrections (table A.1) is not completely accurate, which is supported by the fact that the data points are *not* centered around zero, but around 0.75 pixels and 0.5 pixels respectively.

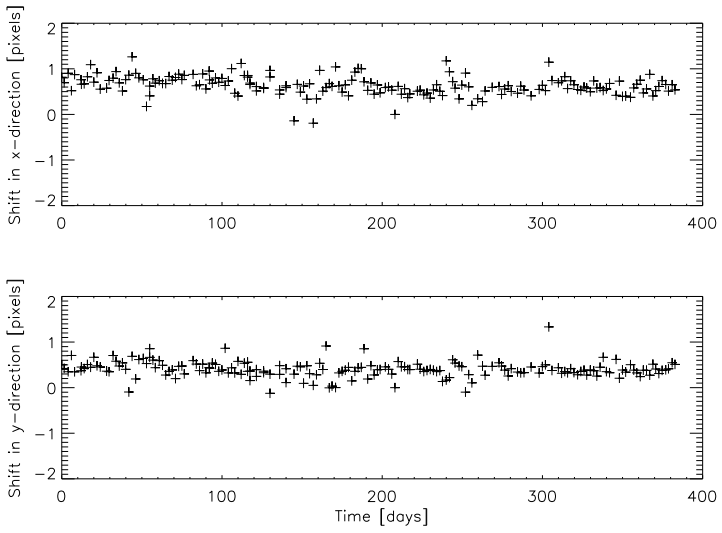

Figure 4.5: The shift between G band and blue continuum in x-direction (*upper panel*) and y-direction (*lower panel*). Start date is 2006-11-12 and end date is 2007-12-02.

4.2.2 Height of the limb in blue continuum

To find the height of the limb in blue continuum (taken at a wavelength around 4504 Å) relative to $\tau_{500} = 1$, MULTI was used with a VAL3C model of the solar atmosphere. MULTI calculated the opacity at 4504 Å as a function of height using the VAL3C atmospheric model. The calculations assume a spherical geometry, and the intensity as a function of radius was found through integration along straight rays that lie tangential to each subsequent sphere with a given radius. The position of the limb was found to be at the height where this intensity has its inflection point. This height was found to be 375 km above $\tau_{500} = 1$.

4.2.3 Difference in limb height between calcium and blue continuum

In calculating the difference in the height of the limb between Ca II H and blue continuum, image series of the synoptic program (program version 52) were used (see Section 3.5.1). In the synoptic program the correlation tracker is not switched on, increasing the jitter in the image series.

The routines used to estimate the fit of the limb uses the method of least squares for calculating a fit. The method of least squares is used as a method to find a fit to a series of data points. To reduce the number of free parameters in the calculation, a routine is used that calculates the distance

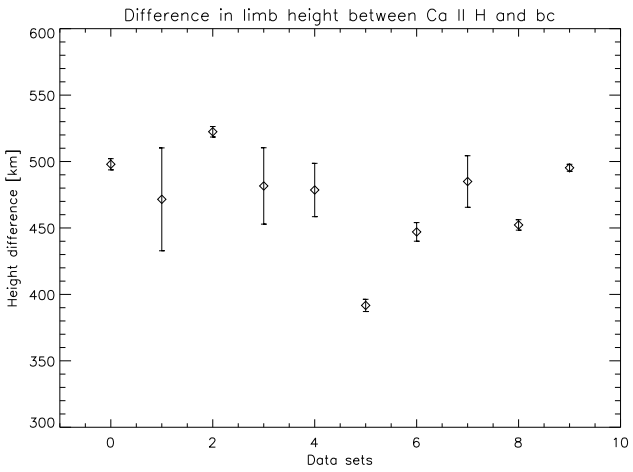

Figure 4.6: Mean difference in limb height between Ca II H and blue continuum for ten different datasets, with error bars $\pm\frac{3\sigma}{\sqrt{n}}$.

from the Earth to the Sun at the date the image was recorded (which is important since the Earth's orbit is slightly elliptic causing the distance to the Sun to vary throughout the year). The solar radius is thus calculated.

In Figure 4.6 the mean difference in height for ten different images series are plotted along with an error $\frac{3\sigma}{\sqrt{n}}$, where σ is the standard deviation and n is the number of data points. In the calculations, a few obvious outliers have been removed. Table 4.1 shows an overview of the datasets with their corresponding means and errors.

Set no.	Date/time	nexp	Mean difference	Error
0	20070109 1613	33	0.498	0.00423
1	20070111 2056	9	0.472	0.0387
2	20070207 0025	44	0.522	0.00394
3	20070209 1104	27	0.482	0.0287
4	20070305 1834	26	0.479	0.0201
5	20070313 1154	44	0.392	0.00461
6	20070525 0533	29	0.447	0.00700
7	20070912 1847	175	0.485	0.0194
8	20071104 1915	91	0.452	0.00392
9	20071110 1123	132	0.495	0.00263

Table 4.1: Mean difference in limb height (in Mm) with error for different datasets (nexp is number of exposures/images).

All heights are measured in Mm (10^6 meters). The mean of the ten

datasets is $\sim (0.472 \pm 0.034)\text{Mm} = (472 \pm 34)\text{km}$.

From the previous calculation of the position of the limb in blue continuum at 375 km above $\tau_{500} = 1$, and the above result, we can thus translate the heights measured relative to the calcium limb in the observations to the standard heights relative to $\tau_{500} = 1$.

Combining the two results, the height of the calcium limb is 847 ± 34 km above $\tau_{500} = 1$.

4.3 Intensity calibration

The intensity of the sunlight that hits the telescope is an unknown factor which cannot be measured directly with observations. The intensity measured with the telescope is affected by the all the optical equipment the light passes through before hitting the detector, as well as the process of interpreting the results from the detector. In order to calculate the incoming intensity, the unknown factor of the telescope's total sensitivity has to be calculated, i.e. how much of the incoming intensity is "lost" on its way to the CCD.

Equation 3.2 shows the different factors involved:

$$N = b \cdot f(t) \cdot S \int I_\nu \Phi(\nu) \mathrm{d}\nu. \tag{4.1}$$

4.3.1 Incoming intensity

Since the incoming (monochromatic) intensity is unknown, intensity from a solar atlas (Brault and Neckel (1987)) is used instead. Because the solar atlas only has the relative intensities, a continuum intensity was calculated using the MULTI software with a FALC model of the solar atmosphere. The continuum intensity was found to be $2.72 \cdot 10^{-5}$ erg cm^{-2} ster^{-1} Hz^{-1}. When integrating over frequency and the transmission filter, we then get

$$\int I_\nu \Phi(\nu) \mathrm{d}\nu = 1.05 \cdot 10^6 \text{ergcm}^{-2} mathrms^{-1} \text{ster}^{-1} \tag{4.2}$$

where I_ν is the intensity from the solar atlas and $\Phi(\nu)$ is the filter transmission as given by the `fg_bfi_filter.pro`-routine (see Section 3.1.3).

4.3.2 The sensitivity of the telescope

Assuming that the intensity of the Sun has remained constant on average since Hinode's first light, it is possible to look at the mean intensity of Hinode observations over time to see if the telescope's total transmission has changed. Hinode/SOT runs a synoptic program each day (program version 52), taking pictures with all six filters, and with otherwise the same

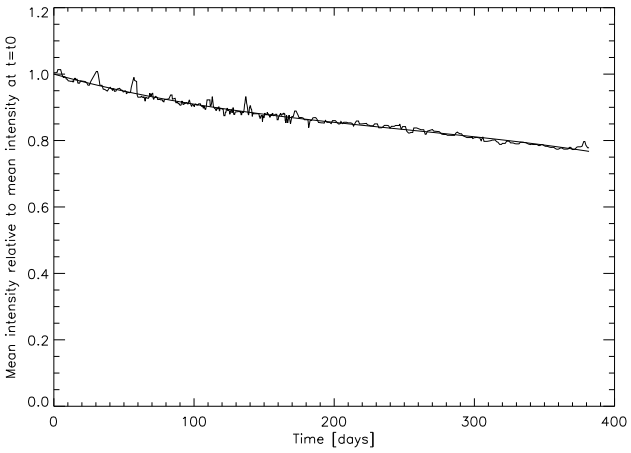

Figure 4.7: Mean intensity relative to the first image, with a polynomial of third degree fit.

specifications. Looking at the calcium images taken with this program, it is possible to see a decline in the mean intensity over time (Figure 4.7).

The images were taken between November 10th 2006 and November 27th 2007, and images with sunspots or other active regions were avoided. The sensitivity decreases almost linearly. The deviations from a linear decrease are assumed to be due to the eclipse season which in this period lasted from May 9th 2007 to August 3rd 2007, see Section 3.1.2. The eclipse season will of course make the temperature in the telescope decrease on average for the duration of the eclipse season. This apparently has consequences for the sensitivity of the instruments.

With a polynomial of third degree fit to the relative sensitivity change with time, we got $f(t) = 1 - 0.001164t + 2.998 \cdot 10^{-6}t^2 - 4.044 \cdot 10^{-9}t^3$, where t is the time.

4.3.3 Efficiency factor

The efficiency factor consists of the remaining unknown, time-independent factors. At $t = 0$ (i.e. the first image from November 10th 2006), the mean counts per second is $N = 1328$ (the mean counts of the image divided with the exposure time, which for the synoptic program is 0.2048 seconds). With the other factors known, the efficiency factor can now be calculated to be $b = 0.00126$ at $t = 0$.

We can now get a plot of how the intensity varies with height, with both the height scale and the intensity scale calibrated, see Figure 4.8.

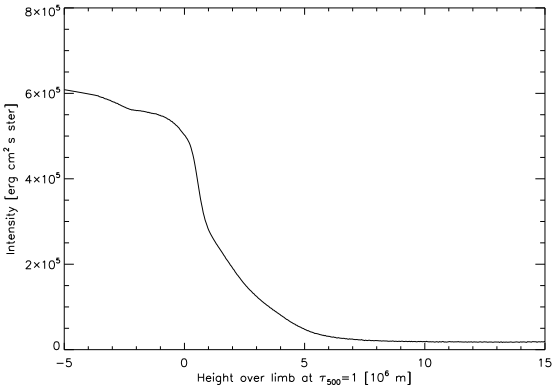

Figure 4.8: The intensity as a function of height above the limb ($\tau_{500} = 1$) for the 20070216_1310-dataset.

4.4 Intensity scale heights

The datasets used for measuring intensity scale heights are listed in Table A.3 in Appendix A. In order to find good datasets in both the equator area and the pole area the search for datasets were widened in respect to the cadence. The cadence is not important for measuring the intensity scale height as the measurement is done on a mean image of the whole time series.

The intensity scale heights are calculated as follows. A routine is used that gives as output the mean of the intensity count in the radial direction from the solar center in all directions in the FoV, i.e. a one-dimensional array. In addition the routine gives as output an array with the distance from the solar center for each pixel outwards. These two arrays correspond to I and z respectively in equation 3.5. An example of how the intensity varies with height is plotted in Figure 4.8. From the disk the intensity drops off steeply at the limb before flattening out at above 5 Mm. The calcium limb is defined by the routine to be where the intensity in calcium has its steepest drop-off (the infliction point), which can be seen to occur right above $z = 0$ (where $\tau_{500} = 1$) at around 500 km. What remains is then to use the built-in routines in IDL to find the logarithm and the derivative of I, and to calculate the scale height according to equation 3.5. This result can then be plotted, see Figure 4.9. In these plots the z-scale has been shifted according to the results in Sections 4.2.2 and 4.2.3. That means that $z = 0$ in these plots is where $\tau_{500} = 1$.

Measuring the scale heights at different latitudes, mainly at the equator and at the poles, there are some distinct features to be seen.

In Figure 4.9 scale heights for different datasets have been plotted according to their heliographical position (west, east, north and south). The

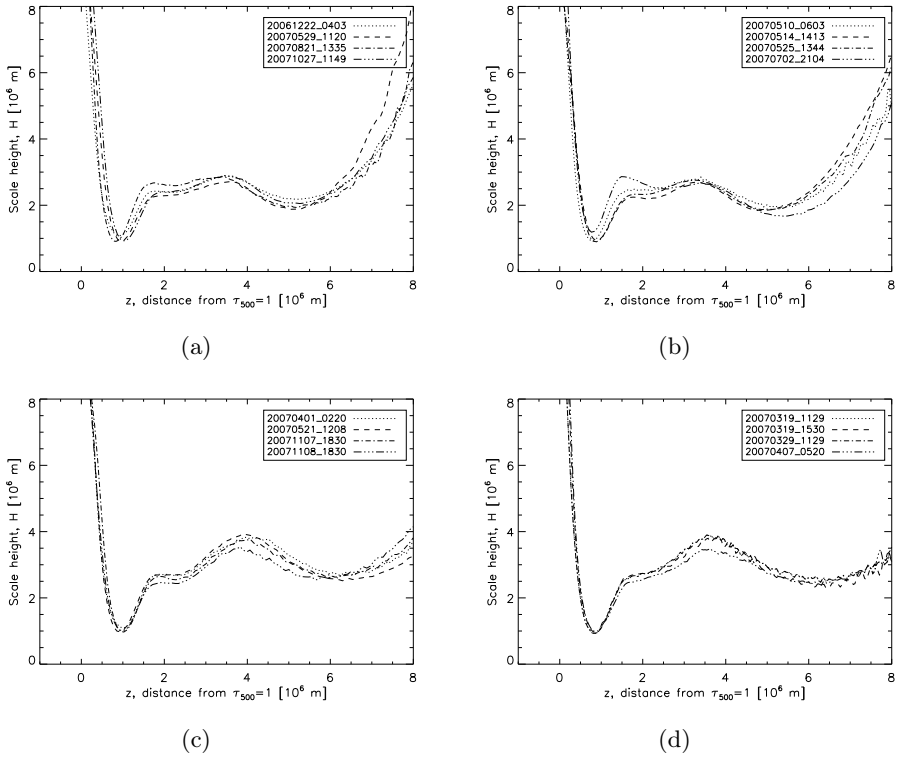

Figure 4.9: Intensity scale heights for different heliographical locations. Figure a) is from the atmosphere to the west, b) to the east, c) to the north and d) to the south.

heliographical directions are traditionally reversed at the equator from what we are used to on Earth, meaning that when looking on the solar disk, west is to the right and east is to the left. On the x-axis we have z, where $z = 0$ is at $\tau_{500} = 1$. In the plots it can be seen that the scale height first declines sharply as the intensity drops off at the limb, reaching a global minimum around the calcium limb at 847 km. From here the scale height takes on a characteristic shape seen for all latitudes where it first rises quickly to a local maximum at a height of about 1.5 Mm where it flattens somewhat before rising to another local maximum around 3.5 Mm. After this second maximum the scale height yet again decreases to a local minimum before rising sharply once more.

A minimum in the scale height corresponds to where the decrease in intensity is at its highest, for example at the limb, and vica versa for maximum. The shape of the intensity scale height then suggest that there may be two populations of spicules with different heights, with dominating at about 1.5 Mm and 3.5 Mm.

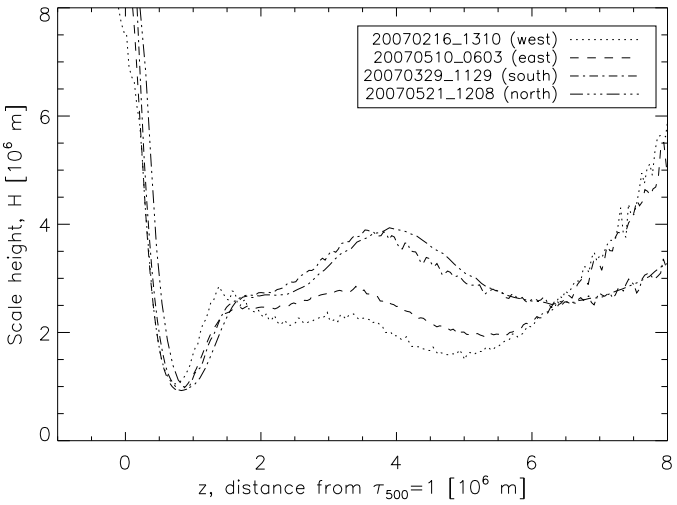

Figure 4.10: Comparison of scale heigths from different heliographical locations.

Above about 8 Mm it is assumed that the main contribution to the intensity is from scattered light from the disk rather than from spicules.

There is a distinct difference between the scale height measured at the equator and at the poles. This can be easily seen in Figure 4.10, where four different scale heights have been plotted, sampled from the western equator, the eastern equator, the south pole and the north pole. The difference arise after the first local maximum where the scale height at the poles clearly is higher than at the equator, with the largest difference being 0.5 Mm occuring at the second local maximum. The second local maximum also appear at somewhat different heights in the atmosphere, with the equator scale height peaking around 2.5 Mm and the pole scale height around 3.5 Mm. This shift between the two latitudes then increases at the second local minimum where the equator scale height has its minimum around a height of 5–5.5 Mm while the pole scale height has its minimum at 6.5 Mm. Here also we can see a difference in the measured scale height of about 1 Mm.

The difference between the equator and the poles are most likely due to the coronal holes that at the poles are responsible for open field lines in the magnetic field, while at the equator the field lines are mainly closed. This will have an impact on how the intensity varies with height.

Since the solar activity since first light of Hinode has been very low, it can be assumed that the intensity from the solar surface that contributes to scattered light in the atmosphere, has been the same for both equatorial and polar regions. (In time periods of high activity, the intensity from the

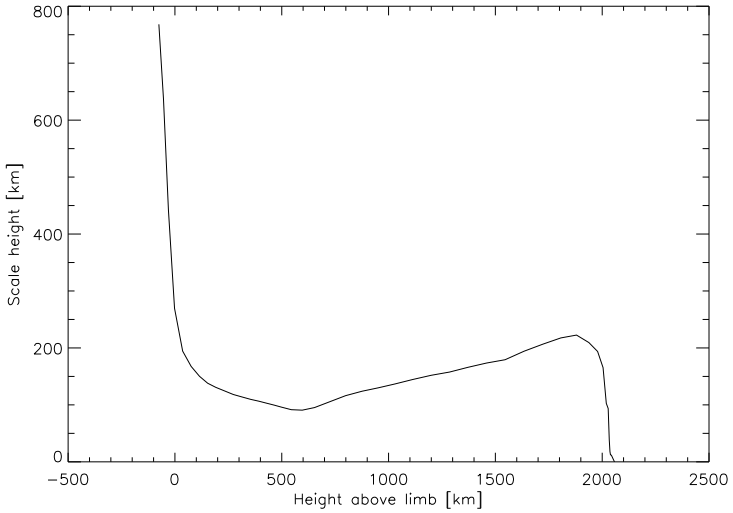

Figure 4.11: The density scale height as simulated by MULTI using a VAL3C atmosphere.

equatorial region will be higher than the polar regions, since solar activity such as sunspots are mainly centered around the equator.) The difference in scale height between the poles and the equator then suggests that the contribution to the intensity from spicules is significant. How much the scattered light contributes to the intensity and the intensity scale heights is unknown.

In Section 2.2.3 the source function for a spicule was defined. By using MULTI with a VAL3C atmospheric model, an estimate of the density scale height can be found, see Figure 4.11. In VAL3C, the chromosphere is defined to end at 2 Mm (which is why the plot of the density scale height is not higher).

It can be seen from this plot that the density scale height lies between 150 and 200 km, with a linear rise. It is clearly not proportional to the intensity scale height, showing that the source function cannot be constant, or the density is far from the density in the VAL3C model or both.

4.5 A visual description of spicules on the limb

Here follows a visual description of spicules on the limb, also including features seen in movies of time series which is otherwise somewhat difficult to include in a written text.

In Figure 4.1, a typical image of spicules on the limb is shown. The contrast between the limb and the disk has been enhanced in order to make

the spicules more visible. To do this a gradient filter was used.

It can be seen from Figure 4.1 that most of the spicules have similar heights, with some individual exceptions. In this image, one spicule in particular stands out with a height of about three times higher than that of those spicules around it. These wide and long spicules have a tendency to fall back down again, while the small, regular ones fade away without falling back.

In Figure 4.3 an example of a rosetta grouping of spicules can be seen. In the figure there are two rosettas, one in the left part of the image and one in the middle. The spicules to the right in the picture do not seem to be grouped like this. Spicules grouped in rosettas are normally brighter than those who are not. Looking at figure 4.1 it can also be seen that rosetta structures are not always present.

4.5.1 Spicules type I

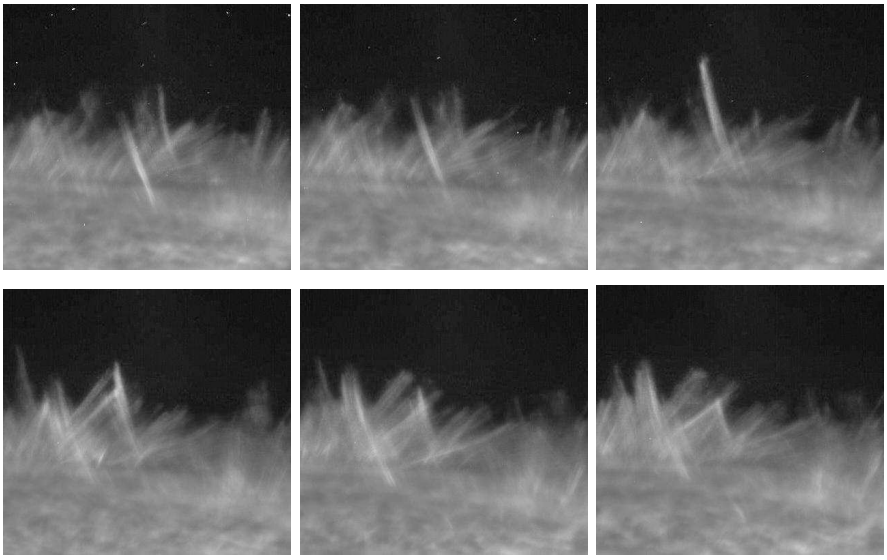

Figure 4.12: Example of spicule type I with visible footpoint.

Spicules of type I are most easily identified due to their movement first upwards and then downwards (while type II have no downward movement). Through visual inspection of time series at different latitudes it is also quite clear that type I is common at low latitudes but rare at the poles (i.e. in coronal holes). Though some downwards movement can be seen at the poles, they are few and far between and it is difficult to see whether they actually are seperate type I spicules or just type II spicules that are replaced by other type II spicules with smaller lengths

In Figure 4.12 a series of images centered on a spicule of type I can be seen. It is clear that it has its footpoint (it originates) on the surface, extends outwards, in this case to twice the height of the background spicules, and falls back again.

4.5.2 Spicules type II

Spicules of type II differ from type I in that they do not seem to fall back down. If this is simply because they loose their energy and fades away or if they are subject to yet another ionization is unkown. The latter would indicate temperatures of ~ 20000 K.

Type II spicules themselves act differently than type I in that they do not necessarily have a distinct top that moves over time but rather that the whole length of the spicule appear at once and the movement itself is best seen as an intensity shift along the spicule. The shape of spicules of type II can also often be seen to change a lot during their individual life times. They may split up to become two or more spicules, their shape may change or they may suddenly deviate from their previous courses. The intensity can have large variations, or the spicule can end up being obscured by other spicules, making it difficult to determine where it ends.

4.6 Measuring the spicules

It is of interest to measure different characteristics of spicules in order to understand the driving mechanisms behind the spicules. These characteristics include lifespans, velocities, accelerations/decelerations (if any), heights and (characteristics of the) intensities.

4.6.1 Choosing a spicule

At first look, an image of the chromosphere in the Ca II H line shows plenty of spicules to choose from. Looking a little closer, single and separate spicules are not necessarily so easy to pick out from the crowd. In addition to not necessarily being well defined along one straight line, there are a lot of noise from the neighbouring spicules, on each side as well as behind.

Due to the noisy background, it is necessary to pick out spicules that are brighter than the neighbouring ones. They may not be the best representative group of spicules.

4.6.2 xt-plots

To easier measure the properties of a single spicule, xt-plots are used. It makes it easier to measure the heights, velocities, durations and acceleration/deceleration (when present). The measurements do have some clear

uncertanties though. As can be seen in Figure **??**, the spicules that are measured are primarily the ones that reach further out than the main population of spicules, making them stand out enough to be visible as individual spicules. The greater part of the spicules do not reach greater heights than the rest, and will thus not stand out enough from "the crowd" to be easily measured. There are a few exceptions of spicules that are brighter than the rest, and can thus be separated due to their brightness instead.

Xt-plots also makes it difficult to measure spicules that change direction during their lifespans.

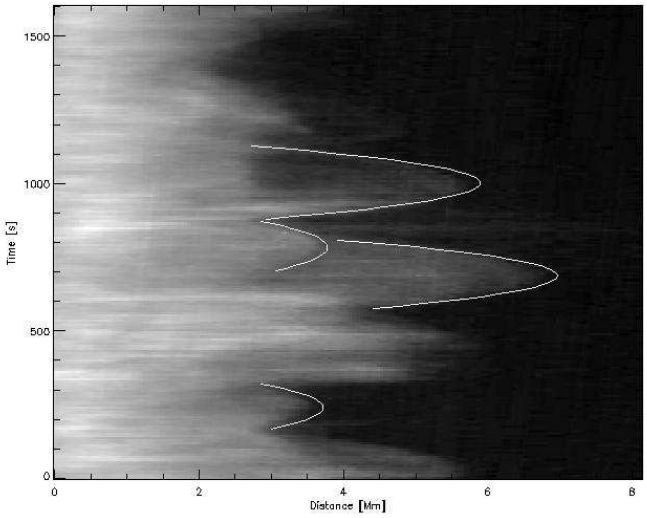

Figure 4.13: xt-plot with several spicules of type I (dotted parabolas).

4.6.3 Type I

When viewing spicules in the Ca II H line, we can see intensity changes that looks like outwards movements, making a straw-like pattern due to the magnetic field lines. It is not known whether we are actually seeing matter that are travelling outwards or if it is something else (temperature changes for example) that causes the apparent outwards movement. Viewing time series as a movie it is possible to see that the spicules also sway from side to side over time, making them look even more like straws swaying in the wind. This makes it slightly more difficult to measure for example the velocity of a spicule, since it does not necessarily follow a straight line.

When the intensities are not important, normalized images have the advantage of bringing out the structures of the solar atmosphere (and smearing out the structures on the uninteresting disk a little), making it easier to measure the characteristics of the spicules.

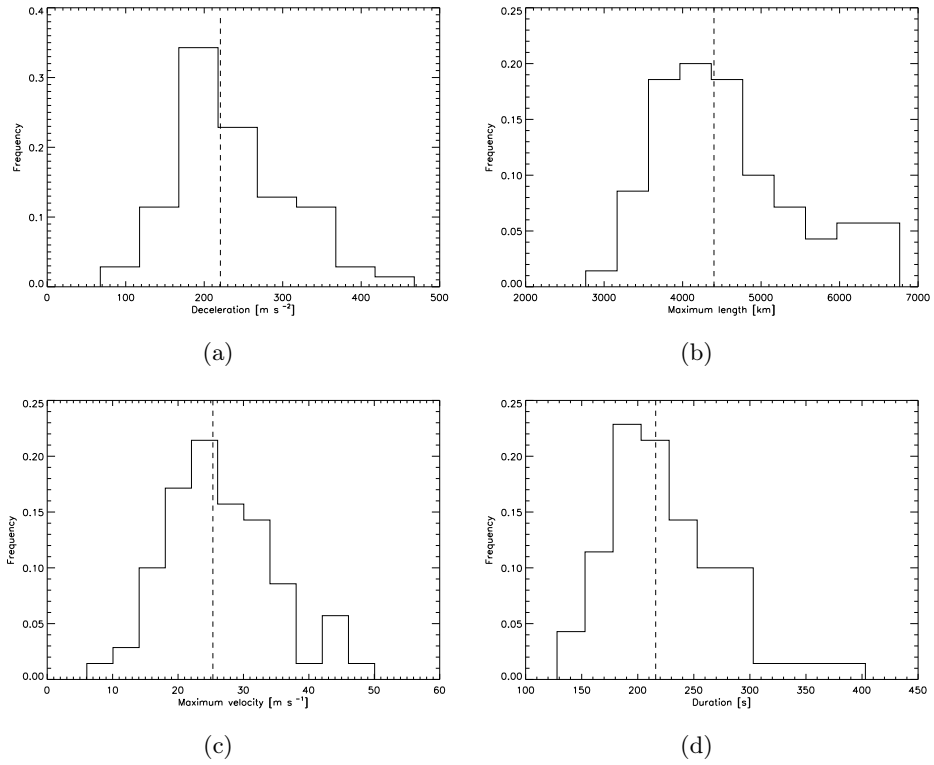

Figure 4.14: Normalized histograms for dataset 20061121_2257, for a) deceleration, b) maximum length, c) maximum velocity and d) duration. The dotted vertical line is the median value for the distribution: a deceleration of 220 m s^{-2}, maximum length of 4400 km, maximum velocity of 25.3 km s^{-1} and duration of 216 seconds.

Type I spicules has as one of its main characteristics that they fall back down into the photosphere. The tip of the spicule will then follow a parabolic path in xt-plots, see Figure 4.13. In order to measure these parabolic paths, a fit to three points was done. The three points were chosen from where the parabola appeared to begin, where it had its top and where it appeared to end.

Using this fit, the maximum velocity can be calculated by taking the maximum value of the derivative, the deceleration can be calculated by taking the double derivative of the fit, the length of the spicule can be estimated by taking the difference between the maximum and minimum points on the fit in the x-direction and the lifetime of the spicule by taking the difference between the maximum and minimum points in the t-direction.

The results of these calculations can be seen plotted as histograms in

Figure 4.14, along with their respective median values. A total of 70 spicules were sampled from the dataset 20061121_2257. The mean value for the deceleration is 232 m s^{-2} with an error $\pm\frac{3\sigma}{\sqrt{n}} = \pm 25.5$m s^{-2}. For maximum length the mean value is 4.55 ± 0.335 Mm, maximum velocity 26.5 ± 3.07 m s^{-1} and duration 225 ± 18.2 s.

De Pontieu et al. (2007b) found lifespans between 180 and 420 seconds, maximum velocities between 10 and 40 m s^{-1} and decelerations between 50 and 400 m s^{-2} when they sampled 20 spicules with parabolic paths, well within the same ranges as the spicules sampled for this thesis.

The length and the lifetime are very much dependent on the choosing of the three points which is done manually. Almost all of the parabolas are found because the spicules are longer than the background of spicules, thus making them stand out against the darker background further up in the chromosphere.

Due to the background of spicules further down, it is unknown whether those spicules measured actually end where they appear to end or whether they continue on down. Most likely it is the last, but extrapolating the parabolas all the way down to the limb does not give any more certain results than just using what is actually visible. The minimum point of the height of the spicules is then the lower of the two points that mark where the parabola begins and ends. From Figure 4.13 it can be seen that the parabolas start well above the limb. In this Figure though, $x = 0$ is where the limb is as seen in Ca II H, and has a small uncertainty due to having being found manually by point-and-click. It is representative for the spicules sampled, that they start and end well above the limb. The length of the spicules may actually be at least 2 Mm longer than what is measured, assuming that all spicules have their footpoints on the surface/limb.

Also, the fact that the spicules measured are more prolonged than the average, poses the question of whether the spicules measured are representative for all the spicules. The few spicules of type I measured that are not prolonged above the average are visible because they have a higher intensity than their surroundings and may then not be representative for the average spicule type I either.

In Figure 4.15 scatter plots comparing each of the four parameters measured to each other, have been plotted. There is a clear linear correlation between deceleration and maximum velocity (0.7, where 1 is full linear correlation and 0 is no correleation at all). Between maximum velocity and maximum length there may be a very weak correlation (0.5), while the remaining four do not seem to have any clear correlation at all (duration and maximum length 0.4, duration and deceleration -0.3, duration and maximum velocity 0.3 and maximum length and deceleration 0.3).

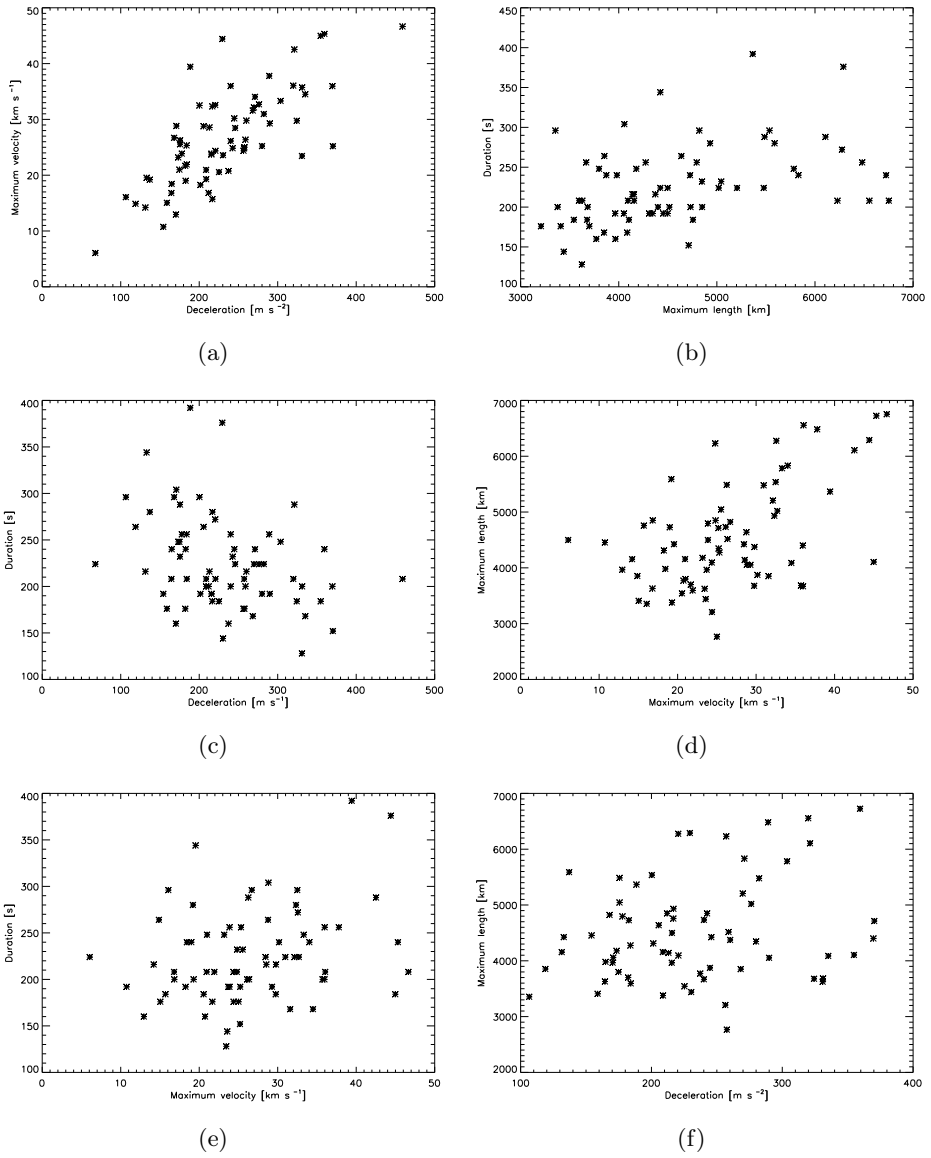

Figure 4.15: Scatter plots of the correlation between a) deceleration and maximum velocity (0.7), b) duration and maximum length (0.4), c) duration and deceleration (-0.3), d) maximum length and maximum velocity (0.5), e) duration and maximum velocity (0.3) and f) maximum length and deceleration (0.3). All plots are for spicules type I from the dataset 20061121_2257.

Comparison to dynamic fibrils

Hansteen et al. (2006), De Pontieu et al. (2007a) and Heggland et al. (2007)

have done a wide analysis of dynamic fibrils from both observations and simulations. What they found were strong evidence for the hypothesis that dynamic fibrils are driven by acoustic shock waves. A constant period means that the shock wave has a fixed time in which the amplitude can go from its maximum to its minimum. This then implies that if there is an increase in maximum amplitude the deceleration has to be larger. For larger periods the wave will have more time between maximum and minimum amplitude which in turn results in lower deceleration. The relation between the deceleration, d, the maximum velocity v_{max} and period P is given by

$$d = \frac{v_{max}}{P/2}. \tag{4.3}$$

The simulations (by Heggland et al. (2007)) showed a near-perfect fit of the data to the theoretical values derived from this formula, giving strong support to this explanation as the driving force behind dynamic fibrils.

The correlations in Figure 4.15 can be compared to the results of De Pontieu et al. (2007a), see Figure 4.16.

It is clear from these scatter plots that spicules type I and dynamic fibrils show the same trend for all the plots, except for a displacement for the plots involving the maximum length.

Most notably, there is a very clear linear correlation between deceleration and maximum velocity, and between deceleration and duration, that is the same for both phenomena. The spicules type I population have a correlation that is slightly higher than for dynamic fibrils. This can be explained by the fact that the spicules type I sampled are to a large degree more extreme cases since they have to "stand out of the crowd" in order to be measured (see discussion above about the weaknesses of the measurement of type I spicules).

The scatter plot of maximum velocity vs. duration shows the same lack of a clear correlation for both dynamic fibrils and spicules type I. However, the plots lie in the same area for both phenomena, showing that also in this they are similar.

In the scatter plots involving maximum length, the greatest differences between dynamic fibrils and spicules type I can be found. Comparing the distribution of maximum length for the two (Figure 4.14 and De Pontieu et al. (2007a)), it is seen that dynamic fibrils range from 0.5 to 3 Mm in length, while spicules type I range from 3 to 7 Mm. This is appearant in that in the scatter plots (the three panels to the right in 4.16), data from the two phenomena are separated. Except for the maximum length, the distributions are very similar between the two. The deceleration and maximum velocity have a little higher, while the duration has a little lower distribution for the spicules, with corresponding shifts in the median values.

The median values for dynamic fibrils were a deceleration of 136 m s^{-2}, maximum length of 1100 km, maximum velocity of 17.8 km s^{-1} and duration

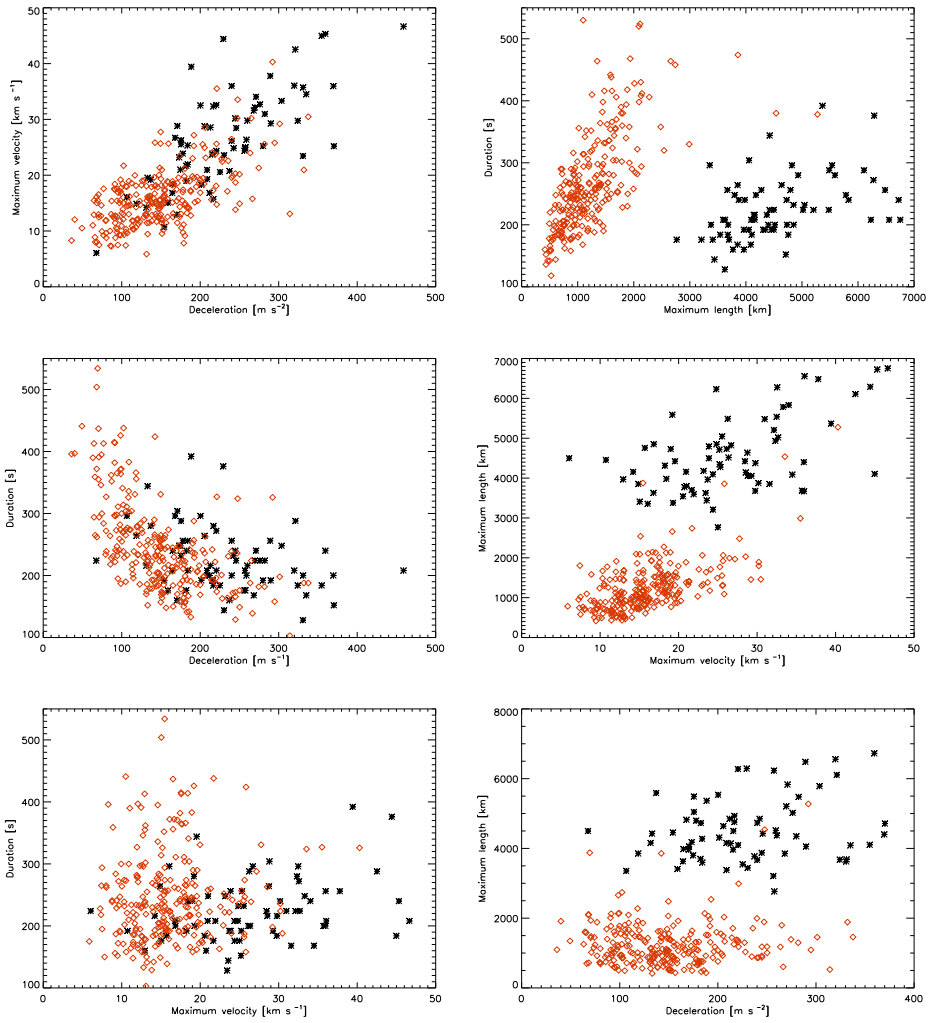

Figure 4.16: Scatter plots of different correlations for dynamic fibrils (*red diamonds*) made by De Pontieu et al. (2007a) to those of spicules type I (*black asterix'*) from Figure 4.15. De Pontieu et al. (2007a) found a clear linear correlation for the upper four panels, deceleration vs. maximum velocity, maximum length vs. duration, deceleration vs. duration and maximum velocity vs. maximum length. For the two lower panels, maximum velocity vs. duration and deceleration vs. maximum length, no clear correlation were found for dynamic fibrils.

of 250 s. The corresponding values for spicules type I are 220 km s^{-1}, 4400 km, 25.3 km s^{-1} and 216 s.

The similar behaviour between dynamic fibrils and spicules type I, prob-

ably means that they most likely have the same driving force behind them. Heggland et al. (2007) showed that acoustic shock waves may drive chromospheric jets, resulting in decelerations that clearly deviates from the gravitational pull of the Sun. The Sun's surface gravity at the equator is 274 m/s^2. It can then be hypothesized that the driving force behind the spicules type I is the same as for dynamic fibrils.

4.6.4 Type II

Measuring type II spicules is a little more complicated than measuring type I spicules. They are harder to identify in xt-plots since they do not have the characteristic parabolic shape of the type I (type II do not fall back into the photosphere). While for type I it was possible to take xt-plots systematically across the limb of a time series, if one wants to measure individual type II spicules, they have to be identified manually in movies before creating xt-plots of the area where the type II spicule are seen to appear.

It is easily seen in the movies that there is a lot of movement outwards, but more difficult to measure with xt-plots since they do not have a shape that is easy to measure on. In xt-plots they usually show up as elongated "blobs" with a clear linear inclination, which mean that they have constant velocity. The inclination with respect to the x-axis indicates how high the velocity is. Steeper inclination means lower velocity. The "blobs", though elongated, rarely has any clear edges, making it difficult to determine where it begins and where it stops. Weaker (or more "normal") type II spicules can be seen in movies but are not easy to detect in the xt-plots. They blend into the background noise too well.

A different approach is thus needed to measure the type II spicules.

Mean velocities

To measure mean velocities the following steps were made. Instead of just looking at one slit made with the xt-plot routine, many slits (50 for summed images and 100 for regular) were extracted, sampling a wider area. The mean was then taken of the resulting xt-plots for each time step, and a routine that measures phase displacements between intensity peaks were employed on the mean image series. By sampling a wider area instead of just one slit, the phase diplacement routine will be able to measure more spicules. This routine simply locates intensity peaks and calculate the displacement these peaks have over time, which is a measure for the velocity (how long it takes to travel a certain distance). The phase displacement is measured between heights that are separated by ten pixels..

The method is dependent on that the spicules in the area used, mainly have the same angle with respect to the limb, and that they have as little transversal movement as possible.

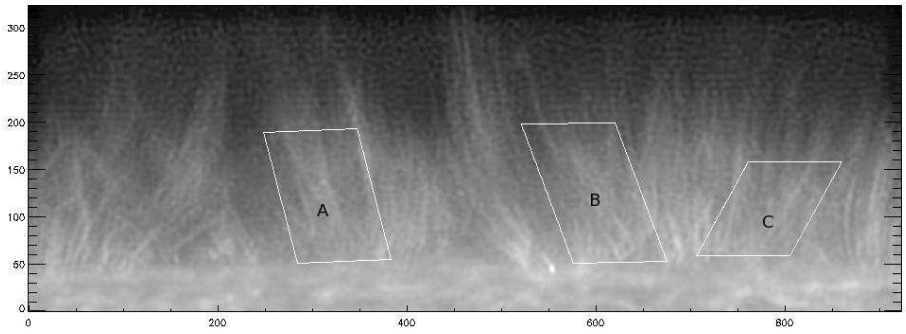

(a) The three areas outlined.

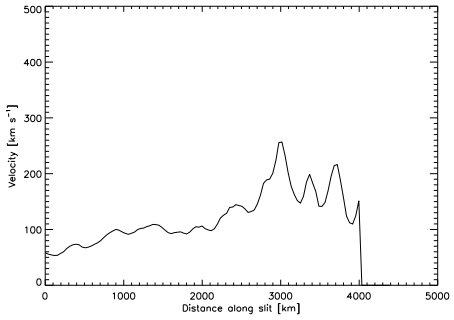

(b) Plot from area A.

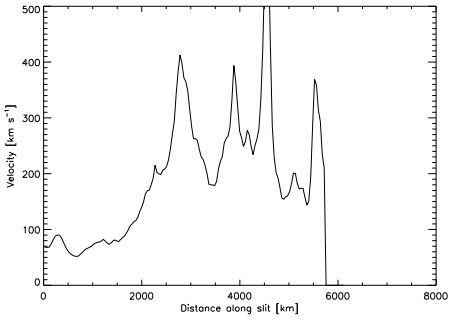

(c) Plot from area B.

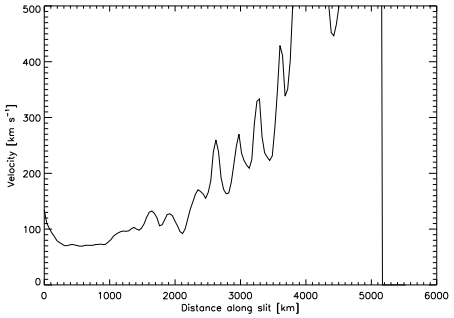

(d) Plot from area C.

Figure 4.17: Mean velocities measured for three different areas from the dataset 20070401_0220.

The resulting output is the mean velocity as a function of height. This method was applied to two different data sets, 20070401_0220 (normal) and 20071107_1830 (summed), with three areas sampled from each data set. In Figures 4.17 and 4.18 the areas sampled are shown on an image taken from the data set as well as the resulting velocity from the different areas. In

Figure 4.19 histograms are plotted for values lower than 400 km s^{-1}, along with their median values.

A velocity of 400 km s^{-1} corresponds to a travel time of 0.5 s to cover ten binned pixels ($10 \cdot 0.0544 \cdot 2 \cdot 725\text{km} = 789\text{km}$). This corresponds to a phase difference ten times smaller than teh cadence of 5 s. This means that any velocities higher than this will be highly uncertain. Also, as the intensity decreases with height, the noise will be responsible for a greater part of the observed intensity.

When this is taken into account, the graphs of mean velocities give an interesting result. The most important feature seen in all graphs except 4.6.4, is that there is an appearant acceleration at the lower part of the atmosphere, from the limb and up to around 2 Mm. The $x = 0$ level in these plots is the lower boundary of the areas that are sampled, and corresponds approximately with where the calcium limb is. The problem with noise is clearly evident in most of the graphs as they get more erratic at greater heights and velocities. There is also the chance that there are spicules with an inclination to the slit that disrupt the phase displacement calculations. The phase displacement routine also has a weakness in that it may measure the phase displacement between two intensity peaks that are from two different spicules instead of one that has moved with time, resulting in velocities that do not actually exist.

Lifetime

Measuring the lifetimes of spicules type II were done manually by looking at movies of two different datasets and counting the number of frames individual spicules were visible. There are two sources of error in this method. The first is due to the cadence or time lapse between each image. For the first dataset, 20070319_1129, the cadence is 4.8 seconds and for the second, 20071107_1830, 5.0 seconds. During the time between each frame, it is unknown whether the individual spicules still exist or not.

The second is due to the measuring method itself being inaccurate. It is assumed that the spicule is actually visible throughout its whole lifetime; that it does not instead disappear because it blends in with the background intensity or that it blends into another spicule so that what is observed is actually two different spicules. It can be seen from the movies that the movement of spicules can be very complex. They may, as previously mentioned, blend into each other, or two spicules may follow very similar paths, making it different to seperate them. Spicules like these have not been included in the measurements. The spicules were chosen so that the uncertainty was kept to a minimum. There were plenty to choose from that did not show this type of behaviour.

There are also quite a number of spicules that do not appear to have any significant velocity outwards. They form appearantly simultaneously along

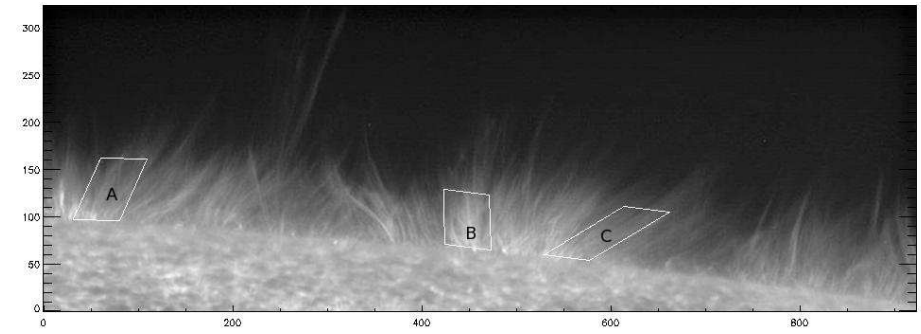

(a) The three areas outlined.

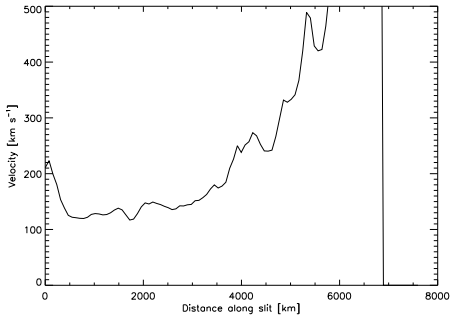

(b) Plot from area A.

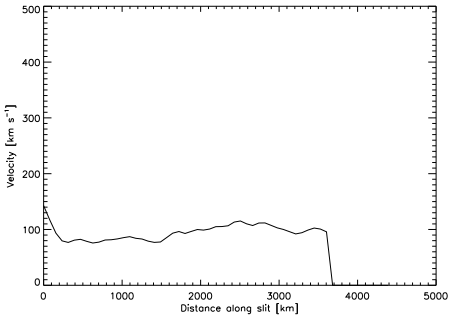

(c) Plot from area B.

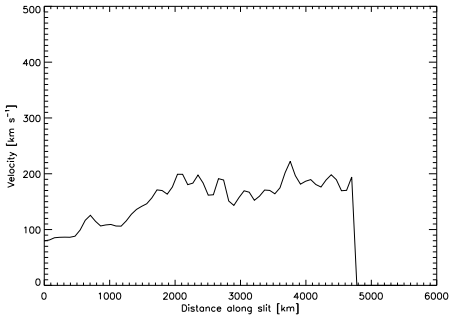

(d) Plot from area C.

Figure 4.18: Mean velocities measured for three different areas from the dataset 20071107_1830.

the whole length of the spicule, and remain static for a relatively long time before fading, again along the whole length. Since these spicules do not show the same dynamic behaviour as the majority, they have also been exluded from the lifetime measurement.

From each of the datasets, a hundred spicules were sampled. The results

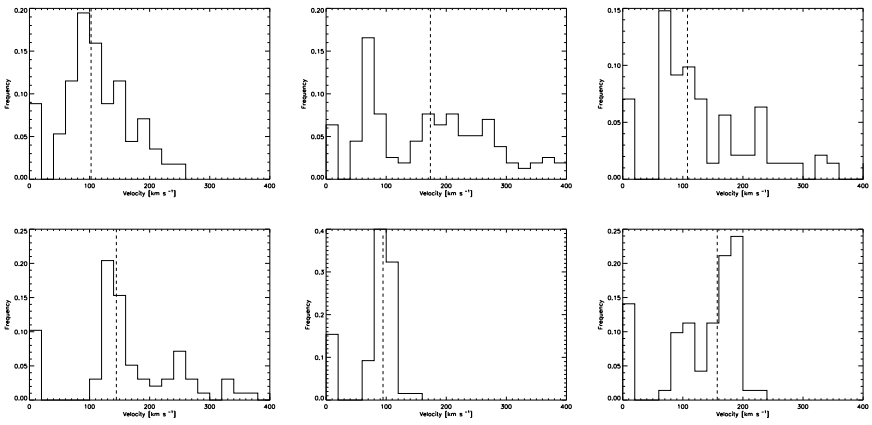

Figure 4.19: Histograms for the mean velocities less than 400 km s^{-1} 20070401_0220_0 (upper panels) and for 20071107_1830 (lower panels). The stipled, vertical lines represent the median values (below 400 km s^{-1}) at 103 km s^{-1}, 174 km s^{-1}, 108 km s^{-1}, 145 km s^{-1}, 95 km s^{-1} and 157 km s^{-1} respectively.

can be seen plotted as histograms in Figure 4.20, along with the median values at 48 seconds and 65 seconds respectively.

For the first dataset, 20070319_1129, the mean value is 55 seconds with an error $\pm\frac{3\sigma}{\sqrt{n}} \approx 7.9$, where σ is the standard deviation. For the second dataset, 20071107_1830, the mean value is 71 with an error $\pm\frac{3\sigma}{\sqrt{n}} \approx 9.2$. This result is similar to that of De Pontieu et al. (2007b), who found the average lifetime of type II spicules in coronal holes to be 45 seconds.

For spicules of type I, the mean value was 225.26 seconds (median value 216.0 seconds), showing another huge difference in the two populations of spicules.

Driving mechanism

De Pontieu et al. (2007b) found that in computer simulations based on acoustic shock wave driving (type I simulations) there were no jets with speeds higher than 50 km s^{-1}. The simulations did not show the rapid fading visible with type II spicules either. It is then highly unlikely that acoustic shock waves are the driving force behind type II.

Another candidate for being the driving mechanism of type II, is magnetic reconnection, which has been a popular theory for the driving mechanism of spicules in general in the past.

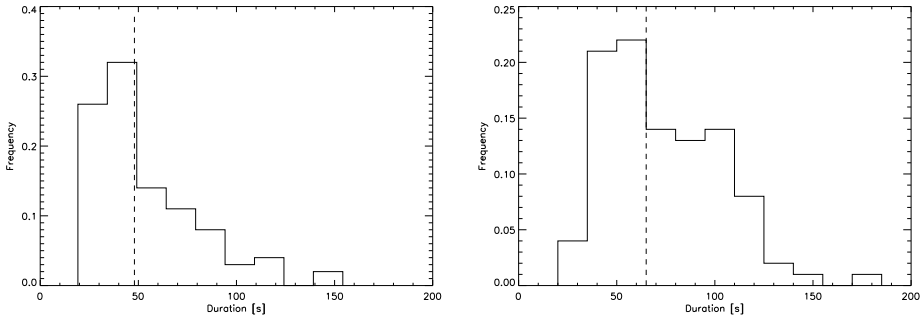

(a) 20070319_1129 (b) 20071107_1830

Figure 4.20: Histogram of the lifetimes of spicules type II. Two datasets were sampled with a hundred spicules each. The stipled vertical line is the median at 48 seconds and 65 seconds respectively.

Chapter 5

Summary and conclusions

The most exciting phrase to hear in science, the one that heralds new discoveries, is not 'Eureka!' (I found it!) but 'That's funny ...'

–Isaac Asimov

5.1 Summary

In this thesis, observations from the Japanes Hinode spacecraft have been used in order to try to understand the solar atmospheric structures known as *spicules* better.

As one of the best solar telescopes in the world today, the observations made with Hinode are important at the cutting edge of solar physics, particularily in the area of the solar atmosphere. The Solar Optical Telescope (SOT) can record data with high resolution and high cadence, and even though its resolution and cadence limit is surpassed by ground-based telescopes, SOT has the advantage of being able to observe the Sun almost continously and without the disturbing turbulence of the Earth's atmosphere degrading the observations. An additional advantage with Hinode, seen from an observer's vantage point, is that all the data recorded with Hinode is freely available to the scientific community.

The SOT has six different filters for observing at different wavelenghts. For this thesis data from the Ca II H-filter were used, since the spectral line this filter is centered around (3968.5 Å) is an important chromospheric spectral line where spicules are clearly visible off the solar limb.

A deep, and time-consuming, dive into the data archives of the SOT was done in order to find datasets (or image series) that could be of interest for observing spicules. A good dataset for observing spicules should span at least ten minutes and have a high cadence (short time between each exposure), preferrably 14 seconds or better. Other good observational criteria that were also taken into account were the exposure time (the longer, the better), the

Field of View (FoV) and whether or not the pixels had gone through an on-board summing before download to Earth.

A total number of 231 datasets were found to fulfill the two main criteria of timespan and cadence. An additional three datasets were later added that did not fulfill the cadence criteria, but these were only used for measurements were cadence was irrelevant. Of these 231 datasets, only about 15 datasets were found good enough for further work.

Data reduction routines were employed on all datasets in order to remove known aberrations. In addition, alignment routines were employed in order to remove jitter from the telescope and for the limb images, a drift caused by the correlation tracker having locked on to disk structures.

In order to be able to measure heights in the atmosphere according to a standard height scale (height relative to where the optical depth at 500 nm equals unity), a calibration of the limb was done. This calibration consisted of several steps. First, the calcium images were compared to blue continuum (centered around 4504 Å). An optical offset caused by the difference in refraction for the two different wavelength-areas were removed, and the remaing difference between the limb in calcium and the limb in blue continuum was determined. Second, the blue continuum limb relative to $\tau_{500} = 1$ was determined with the help of a computer simulation, using the simulation software MULTI with a much used model of the solar atmosphere, VAL3C. The height of the calcium limb above $\tau_{500} = 1$ was thus found to be 847 km.

Since the telescope only returns a data number from the CCD instead of an intensity in useful units, a calibration of the intensity was done. This calibration is time dependent, since the sensitivity of the telescope decreases with time. By determining the time-independent constants and the time-dependent sensitivity of the telescope, an intensity calibration were done.

As a tool for looking at how the intensity changes with height above the limb, intensity scale heights were calculated for a number of data sets, taken at different heliographical positions. The results clearly show a difference between the equatorial and polar regions. At the poles, the magnetic field lines are open due to constant coronal holes. As a result, the spicules will stretch higher into the atmosphere at the poles. The scale height values are also up to 1 Mm higher at the poles than above the equator. The intensity scale heights give an indication that there might be two different populations depending on the length of the spicules.

In addition to knowing how the intensity varies with height for spicules, it is also of interest to measure their lifetimes, maximum lengths, maximum velocities and accelerations/decelerations. There are two main types of spicule populations, type I and II. Type I are characterised by having a parabolic path with respect to time (they have both upwards and downwards movement), while type II only moves upwards and fades away (in Ca II H). There are also other differences. Type I has a longer lifespan than type II, lasting typically around 225 seconds while type II last typically around 50

seconds. And while type I experience a deceleration througout its lifespan, type II seem to be accelerated at least in the lower part of the chromosphere. This indicate that there are two different driving mechanism behind the two types of spicules. It has been hypothesized that type I are driven by acoustic shock waves, while type II are driven by magnetic reconnection.

5.2 Further work

There are several things to be taken into consideration for further work and studies of spicules. Good computer simulations and better observations will be important.

With the data already available from Hinode, an important next step will be to create good routines for measuring a large number of spicules automatically. Especially in the areas where the measurements in this thesis have been done manually, such as the lifetimes of spicules type II. With more automatic routines, a larger statistic population of the measured characteristics can be made. Better comparisons of different areas (quiet Sun, active region, coronal hole) could also be done.

It would also be useful to get a measure of how much of the intensity in the atmosphere is due to scattered light, in order to measure the real intensity of the spicules.

In order to understand what phenomena that drives the spicules, good computer models will have to be developed with which the results can be compared to the observational data.

5.2.1 Observations

Even though Hinode offers some of the best observations we have of the Sun so far, there is still need of better telescopes and instruments. The SOT observations of spicules are at the very limit of the resolution limits of the telescope.

The limited bandwidth for downloading the data from the satellite also limits the frequency, or cadence, of the exposures.

Both limitations affect the observations of spicules. Their widths are at the resolution limit, and with higher resolution we will probably be able to see even more spicules that are so small that today's telescopes cannot discern them. Spicules, particularily of type II, are very dynamic and changes in a matter of seconds. Better time resolution (cadence) will give better understanding of how spicules evolve.

Upcoming projects

There are several telescopes under development that will bring us the next step on the way.

GREGOR is a new ground-based, German solar telescope with a 1.5 meter aperture (Balthasar et al. (2007)), located at Tenerife. First light of the telescope is planned for the beginning of 2009. GREGOR is designed as an open air telescope, so that the air can flow freely through the telescope. It will be fitted with adaptive optics that is designed to remove the effects of seeing from the images.

SUNRISE is a German-led, balloon-borne solar telescope (Barthol et al. (2008)) with 1 m aperture, with a planned flight for the summer of 2009. The main scientific goal is to study and understand the structure and dynamics of the magnetic field in the solar atmosphere. Using a balloon to bring the telescope above most of the atmosphere, it will provide near-diffraction limitied images with a resolution down to 35 km on the solar surface.

Solar Dynamics Observatory[1] is the next space-born mission from NASA, and is a part of NASA "Living With a Star" program. It is currently scheduled for launch in January 2010. SDO's goal is to better understand the solar influence on Earth, with particular focus on understanding the Sun's magnetic field.

ATST (the Advanced Technology Solar Telescope) is a 4 m telescope under development in the USA (Rimmele and the ATST team (2008)). It will probably see first light in 2012, and will have a resolution of only 0."03 (corresponding to 20 km on the Sun) in visible light. The ATST will be ground-based and situated on Haleakala on Maui.

Solar Orbiter is a space-born mission in development at ESA (European Space Agency), with a planned launch in 2015 at the earliest (Marsden and Fleck (2007)). The spacecraft will be sent into an orbit that will be making both very close passes to the Sun ($\approx$ 22 AU) and also high-latitude passes. It will then be able to observe the properties, dynamics and interactions of the solar surface, atmosphere and the inner heliosphere.

Solar-C is the next generation of space-born solar telescope from the japanese space agency (JAXA)[2]. It has a preliminary planned launch in 2016 and is still very much at the planning stage. One of the two suggested choices ("Plan B") will give high resolution and high cadence spectroscopic and X-ray observations of the whole solar atmosphere if it ends up beeing chosen.

One of the main problems with ground-based observation is that the adaptive optics necessary for making good observations usually are optimized for observations on the disk, making it difficult to obtain good data of the solar limb from the ground. Attempts to obtain good observations of the solar limb with the Swedish Solar Telescope on La Palma has so far not been successful.

Space-born telescopes are vitally important for observing the solar at-

[1] http://sdo.gsfc.nasa.gov/

[2] http://solar-b.nao.ac.jp/SOLAR-C/index_e.html

mosphere at high resolution as long as seeing continues to be a problem for ground-based observations.

Appendix A

Tables

Wave	rot	xshift	yshift	xscale	yscale
3883 (CN)	0.0000	0.94	-6.23	1.00041	1.00041
3968 (Ca II H)	0.0000	-1.35	-5.24	1.00021	1.00021
4305 (G-band)	0.0000	0.00	0.00	1.00000	1.00000
4504 (Blue cont.)	0.0000	1.34	6.49	0.99921	0.99921
5550 (Green cont.)	0.0000	-0.36	3.03	0.99497	0.99497
6684 (Red cont.	0.0000	0.60	-1.38	0.99140	0.99140

Table A.1: The offset on the detector created by the optical layout.

Date/time	FoV	Binned	CT on	Other
20070109 1613	4096x2048	Yes	No	Quiet Sun, North
20070111 2056	4096x2048	Yes	No	Quiet Sun, North
20070207 0025	4096x2048	Yes	No	Sun spot on disc, west
20070209 1104	4096x2048	Yes	No	Sun spot on disc, west
20070305 1834	4096x2048	Yes	No	
20070313 1154	4096x2048	Yes	No	
20070525 0533	2048x2048 (x0=1025)	Yes	No	
20070723 1213	1024x1024 (x0=2048)	No	No	
20070912 1847	2048x2048 (x0=1024)	Yes	No	
20071110 1123	2048x2048 (x0=1025)	Yes	No	
20071104 1915	2048x2048 (x0=1025)	Yes	No	

Table A.2: Data sets used for calculating the difference in limb height between Ca II H and blue continuum.

Date/time	FoV	Binned	Direction
20070117 1210	512x1024	No	South
20070216 1310	1024x2048	No	West
20070319 1129	1024x1024	No	South
20070319 1530	1024x1024	No	South
20070401 0220	1024x1024	No	North
20070407 0520	1024x1024	No	South
20070510 0603	1024x2048	No	East
20070521 1208	512x1024	Yes	North
20070525 1344	512x1024	Yes	East
20070529 1120	1024x1024	Yes	West
20070702 2104	512x1024	Yes	East
20070821 0130	1024x1024	Yes	West
20071027 1149	1024x1024	Yes	West
20071108 1830	1024x1024	Yes	North

Table A.3: Data sets used to measure the scale height.

Appendix B

Data sets

Date/time	Cad.	nx	ny	Sum.	exp	nexp	Min.	x	y	mu	Limb	Orien.
20061115 1910	8.0	1024	1024	No	0.20	447	59.5	302	-125	1.23	No	
20061117 0742	9.9	1024	1024	No	0.21	938	154.2	622	-114	0.92	No	
20061118 1045	8.0	1024	1024	No	1.02	776	103.4	777	-113	0.76	No	
20061119 2258	5.0	1024	2048	No	0.51	522	43.4	934	-97	0.60	Yes	West
20061120 1119	8.0	1024	1024	No	0.51	1316	175.4	960	-89	0.58	Yes	West
20061121 0111	8.0	1024	1024	No	0.51	896	119.4	960	-89	0.58	Yes	West
20061121 0715	5.0	1024	2048	No	0.51	594	49.4	960	-89	0.58	Yes	West
20061121 2257	8.0	1024	1024	No	0.51	1518	202.3	960	-89	0.58	Yes	West
20061122 0000	8.0	1024	1024	No	0.51	1050	139.9	960	-89	0.58	Yes	West
20061122 0557	5.0	1024	2048	No	0.51	450	37.4	960	-89	0.58	Yes	West
20061127 1315	5.0	1024	2048	No	0.51	712	59.3	900	-399	0.56	Yes	South-west

Date/time	Cad.	nx	ny	Sum.	exp	nexp	Min.	x	y	mu	Limb	Orien.
20061127 1632	5.0	1024	2048	No	0.51	567	47.2	900	-399	0.56	Yes	South-west
20061127 1809	5.0	1024	2048	No	0.51	423	35.2	900	-399	0.56	Yes	South-west
20061128 0448	5.0	1024	2048	No	0.51	795	66.2	899	-399	0.56	Yes	South-west
20061128 0939	5.1	1024	2048	No	0.51	400	34.1	900	-399	0.56	Yes	South-west
20061128 1352	5.0	2048	1024	No	0.51	604	50.2	0	924	0.62	No	
20061128 1952	5.0	2048	1024	No	0.51	568	47.3	0	924	0.62	No	
20061205 1930	8.0	1024	1024	No	0.51	672	89.5	809	-167	0.72	No	
20061206 1114	10.0	2048	1024	Yes	0.13	723	120.4	-867	-92	0.68	No	
20061206 2010	10.0	2048	1024	Yes	0.13	1257	209.4	-826	-92	0.72	No	
20061218 1121	8.0	1024	1024	Yes	0.15	2083	277.7	998	-97	0.54	Yes	West
20061218 1608	8.0	1024	1024	Yes	0.15	5382	717.7	998	-97	0.54	Yes	West
20061219 0415	8.0	1024	1024	Yes	0.15	2564	341.8	998	-97	0.54	Yes	West
20061221 0020	10.0	2048	1024	Yes	0.13	537	89.4	0	940	0.61	Yes	North
20061222 0403	8.0	1024	1024	Yes	0.15	1324	176.5	980	0	0.57	Yes	West
20061223 1123	10.0	2048	1024	Yes	0.51	1641	273.4	605	780	0.56	Yes	North-east
20061223 1636	10.0	2048	1024	Yes	0.51	1833	305.4	605	780	0.56	Yes	North-east
20061224 0000	11.1	2048	1024	Yes	0.51	1158	214.4	605	780	0.56	Yes	North-east
20061224 0540	10.0	2048	1024	Yes	0.51	1554	258.9	605	780	0.56	Yes	North-east
20061224 1200	10.2	2048	1024	Yes	0.51	1321	223.4	605	780	0.56	Yes	North-east
20070109 2314	14.7	512	2048	No	0.77	614	149.9	821	-28	0.73	No	
20070111 1105	8.1	1024	1024	Yes	0.15	1436	194.5	1015	-43	0.53	Yes	West
20070111 2301	8.0	1024	1024	Yes	0.21	1346	179.4	960	-43	0.59	Yes	West
20070112 0454	8.0	1024	1024	Yes	0.21	2237	298.4	960	-43	0.59	Yes	West

Date/time	Cad.	nx	ny	Sum.	exp	nexp	Min.	x	y	mu	Limb	Orien.
20070112 2330	9.1	1024	1024	Yes	0.21	1671	254.4	898	-98	0.64	Yes	West
20070113 0530	8.0	1024	512	No	0.10	640	85.3	917	-102	0.63	No	
20070113 2245	10.0	1024	1024	Yes	0.21	1797	299.4	956	-113	0.58	Yes	West
20070114 0359	10.0	1024	1024	Yes	0.21	2157	359.5	956	-113	0.58	Yes	West
20070114 1018	10.0	1024	1024	Yes	0.21	609	101.4	956	-113	0.58	Yes	West
20070114 1210	12.0	512	2048	No	0.51	548	109.5	956	-113	0.58	Yes	West
20070117 1210	12.0	512	2048	No	0.51	1747	349.3	0	-945	0.60	Yes	South
20070118 1214	12.1	512	2048	No	0.51	1710	344.3	0	-944	0.60	Yes	South
20070125 0028	10.0	1024	1024	Yes	0.21	1887	314.4	1015	70	0.53	Yes	West
20070125 0557	10.2	1024	1024	Yes	0.21	1791	305.4	1016	70	0.53	Yes	West
20070126 0015	8.0	1024	1024	No	0.21	2580	344.0	960	-71	0.58	Yes	West
20070126 0615	8.4	1024	1024	No	0.21	1852	258.4	960	-71	0.58	Yes	West
20070126 1825	8.0	1024	1024	No	0.21	1609	214.5	-949	-69	0.59	No	
20070127 0025	8.0	1024	1024	No	0.21	883	117.6	-949	-69	0.59	No	
20070127 0223	8.0	1024	1024	No	0.21	775	103.2	-949	-69	0.59	No	
20070127 0406	8.0	1024	1024	No	0.21	772	102.8	-949	-69	0.59	No	
20070127 0549	8.0	1024	1024	No	0.21	255	33.9	-949	-69	0.59	No	
20070127 0643	8.0	1024	1024	No	0.21	923	123.0	-949	-69	0.59	No	
20070127 0846	8.0	1024	1024	No	0.21	560	74.6	-949	-69	0.59	No	
20070127 1208	8.0	1024	1024	Yes	0.21	1499	199.8	-914	-42	0.63	No	
20070127 1527	8.0	1024	1024	Yes	0.21	1208	161.0	-901	-39	0.65	No	
20070206 1554	11.2	512	512	No	0.10	645	120.0	514	482	0.85	No	
20070206 2005	8.0	1024	1024	Yes	0.21	1842	245.6	905	-46	0.64	No	

Date/time	Cad.	nx	ny	Sum.	exp	nexp	Min.	x	y	mu	Limb	Orien.
20070207 0825	8.0	1024	1024	Yes	0.21	1342	178.8	940	-58	0.60	Yes	West
20070207 1225	8.0	1024	1024	Yes	0.21	2373	316.3	950	-39	0.59	Yes	West
20070207 1801	8.0	1024	1024	Yes	0.21	2688	358.4	949	-39	0.59	Yes	West
20070208 0013	8.0	1024	1024	Yes	0.21	2595	346.0	950	-39	0.59	Yes	West
20070208 0618	8.0	1024	1024	Yes	0.21	1208	161.0	950	-39	0.59	Yes	West
20070208 1140	8.0	1024	1024	Yes	0.31	2850	380.0	980	-39	0.56	Yes	West
20070208 1814	8.0	1024	1024	Yes	0.31	1423	189.6	980	-39	0.56	Yes	West
20070209 0013	8.0	1024	1024	Yes	0.31	2745	366.0	980	-39	0.56	Yes	West
20070209 0633	8.0	1024	1024	Yes	0.31	1513	201.7	980	-39	0.56	Yes	West
20070209 1005	8.0	1024	1024	Yes	0.31	334	44.4	980	-39	0.56	Yes	West
20070209 1143	8.0	1024	1024	Yes	0.31	2861	381.4	980	-40	0.56	Yes	West
20070209 1819	8.0	1024	1024	Yes	0.31	2505	334.0	980	-39	0.56	Yes	West
20070210 0007	8.0	1024	1024	Yes	0.31	2598	346.4	980	-39	0.56	Yes	West
20070210 0607	8.0	1024	1024	Yes	0.31	1635	217.9	980	-39	0.56	Yes	West
20070213 0430	10.0	512	512	No	0.10	574	95.5	136	-311	1.22	No	
20070214 0915	8.0	1024	2048	No	0.51	448	59.6	777	-153	0.76	No	
20070215 0030	11.2	512	512	No	0.31	645	120.0	737	-248	0.77	No	
20070216 1132	11.2	512	512	No	0.31	524	97.5	939	-193	0.58	Yes	West/South-west
20070216 1310	11.2	1024	2048	No	0.51	476	88.5	939	-193	0.58	Yes	West/South-west
20070217 0750	11.2	1024	2048	No	0.51	401	74.5	638	117	0.90	No	
20070217 1235	11.2	512	512	No	0.31	932	174.4	-5	0	1.57	No	
20070218 2020	11.2	512	512	No	0.31	427	79.4	852	85	0.69	No	
20070219 1341	11.2	1024	2048	No	0.51	664	123.6	282	-32	1.28	No	

Date/time	Cad.	nx	ny	Sum.	exp	nexp	Min.	x	y	mu	Limb	Orien.
20070219 1918	11.2	512	512	No	0.31	757	140.9	-26	0	1.54	No	
20070219 2241	8.0	1024	512	No	0.41	518	68.9	14	0	1.56	No	
20070220 1155	8.0	1024	512	No	0.41	765	101.8	-461	-62	1.09	No	
20070220 1825	8.0	1024	512	No	0.41	765	101.8	-407	-59	1.15	No	
20070220 2100	11.2	1024	2048	No	0.51	346	64.3	-386	-57	1.17	No	
20070221 0710	4.0	1024	1024	No	0.51	1043	69.5	-298	-53	1.26	No	
20070222 0800	4.0	1024	1024	No	0.51	818	54.5	440	-100	1.11	No	
20070222 1211	8.0	400	1024	No	0.41	765	101.8	107	-64	1.44	No	
20070223 0048	11.2	1024	2048	No	0.51	473	88.0	221	-66	1.33	No	
20070223 1852	4.0	1024	1024	No	0.51	885	58.9	361	-74	1.19	No	
20070223 1901	4.0	1024	1024	No	0.51	1282	85.4	169	-65	1.38	No	
20070224 0052	11.2	1024	2048	No	0.51	481	89.5	412	-76	1.14	No	
20070224 1206	6.4	1024	512	No	0.41	765	81.4	503	-82	1.05	No	
20070224 1856	4.0	1024	1024	No	0.51	893	59.5	555	-87	0.99	No	
20070225 0100	11.2	1024	2048	No	0.51	403	74.9	599	-91	0.95	No	
20070225 0351	7.0	1024	512	No	0.41	506	58.8	619	-93	0.93	No	
20070225 1121	11.2	1024	2048	No	0.51	1125	209.5	670	-98	0.87	No	
20070225 1955	4.0	1024	1024	No	0.51	885	58.9	724	-106	0.82	No	
20070226 0059	11.2	1024	2048	No	0.51	480	89.6	753	-110	0.79	No	
20070226 1240	4.0	1024	1024	No	0.51	1043	69.5	814	-121	0.72	No	
20070226 1901	11.2	1024	2048	No	0.51	1318	245.4	842	-127	0.69	No	
20070227 0334	11.2	512	512	No	0.31	641	119.3	4	0	1.57	No	
20070228 0830	4.0	1024	1024	No	0.51	818	54.5	-70	15	1.50	No	

Date/time	Cad.	nx	ny	Sum.	exp	nexp	Min.	x	y	mu	Limb	Orien.
20070228 1505	4.0	1024	1024	No	0.51	1237	82.4	-22	17	1.54	No	
20070301 0014	6.4	1024	512	No	0.41	765	81.4	63	17	1.50	No	
20070301 2100	8.0	1024	1024	No	0.51	598	79.5	254	13	1.31	No	
20070303 0735	11.2	512	512	No	0.31	703	130.8	0	0	1.57	No	
20070303 1120	11.2	512	512	No	0.31	1178	219.4	581	-6	0.97	No	
20070303 1500	8.0	1024	1024	No	0.51	1331	177.1	608	-9	0.94	No	
20070303 1812	8.0	1024	1024	No	0.51	809	107.6	631	-11	0.92	No	
20070303 1959	8.0	1024	1024	No	0.51	809	107.6	631	-11	0.92	No	
20070304 1107	11.2	512	512	No	0.31	1167	217.3	741	-25	0.80	No	
20070305 0548	6.4	1024	512	No	0.41	765	81.4	0	0	1.57	No	
20070305 2136	8.0	1024	1024	No	0.51	891	118.5	901	-60	0.64	No	
20070309 0316	6.4	1024	512	No	0.41	7657	81.4	1	0	1.57	No	
20070311 0500	4.8	1024	1024	No	0.51	741	59.1	680	680	0.58	No	
20070311 1404	11.2	512	512	No	0.31	1262	235.0	-574	61	0.97	No	
20070318 0634	6.4	1024	512	No	0.41	765	81.4	27	0	1.54	No	
20070318 0918	6.4	1024	512	No	0.41	301	31.9	52	0	1.52	No	
20070319 1129	4.8	1024	1024	No	0.51	758	60.5	0	-967	0.57	Yes	South
20070319 1530	4.8	1024	1024	No	0.51	745	59.4	0	-967	0.57	Yes	South
20070323 0351	6.4	1024	512	No	0.41	765	81.4	89	0	1.48	No	
20070324 0806	6.4	1024	512	No	0.41	504	53.6	-593	128	0.94	No	
20070324 1813	6.4	1024	512	No	0.41	765	81.4	-516	134	1.02	No	
20070324 2057	6.4	1024	512	No	0.41	352	37.4	-494	136	1.04	No	
20070325 0614	11.3	512	512	No	0.31	677	127.0	-418	141	1.11	No	

Date/time	Cad.	nx	ny	Sum.	exp	nexp	Min.	x	y	mu	Limb	Orien.
20070325 1456	6.4	1024	512	No	0.41	765	81.4	-343	144	1.18	No	
20070326 0019	11.2	512	512	No	0.31	859	160.4	-259	147	1.26	No	
20070326 1721	6.7	1024	1024	No	0.51	531	59.5	-134	151	1.36	No	
20070326 2021	6.4	1024	512	No	0.41	765	81.4	-75	151	1.40	No	
20070327 0400	11.3	512	512	No	0.31	503	94.3	-3	151	1.41	No	
20070327 0631	6.4	1024	512	No	0.41	765	81.4	19	151	1.41	No	
20070328 0301	6.4	1024	512	No	0.41	765	81.4	210	147	1.30	No	
20070331 0014	6.4	1024	1024	No	0.51	991	105.4	-558	206	0.95	No	
20070331 0259	11.3	512	512	No	0.21	273	51.2	-505	208	1.00	No	
20070331 0356	11.3	512	512	No	0.21	801	150.1	-498	208	1.01	No	
20070331 0641	6.4	1024	1024	No	0.51	738	78.5	-507	210	1.00	No	
20070331 0800	11.2	512	512	No	0.21	650	121.3	-465	210	1.04	No	
20070401 0220	4.8	1024	1024	No	0.51	616	49.1	0	945	0.59	Yes	North
20070401 0650	11.2	512	512	No	0.21	1306	244.1	-270	219	1.21	No	
20070401 1110	4.8	1024	1024	No	0.51	678	54.1	0	-945	0.59	Yes	South
20070401 1209	4.8	1024	1024	No	0.51	691	55.1	614	-717	0.59	Yes	South-west
20070401 1309	4.8	1024	1024	No	0.51	691	55.1	803	-495	0.59	Yes	South-west
20070401 1409	4.8	1024	1024	No	0.51	691	55.1	900	-288	0.59	Yes	South-west
20070401 1509	4.8	1024	1024	No	0.51	691	55.1	933	-145	0.59	Yes	South-west
20070401 1609	4.8	1024	1024	No	0.51	521	41.5	360	-889	0.57	Yes	South/South-west
20070401 1855	11.2	512	512	No	0.21	1627	303.0	-161	221	1.29	No	
20070407 0520	4.8	1024	1024	No	0.51	1517	121.1	0	-970	0.56	Yes	South
20070408 1840	10.0	1024	1024	Yes	0.31	657	109.3	0	-960	0.57	Yes	South

Date/time	Cad.	nx	ny	Sum.	exp	nexp	Min.	x	y	mu	Limb	Orien.
20070409 0618	10.0	1024	1024	Yes	0.31	969	161.4	-960	0	0.57	Yes	East
20070410 1124	11.2	512	512	No	0.21	1745	325.1	-168	650	0.87	No	
20070424 1305	15.0	1024	1024	Yes	0.15	1102	275.3	790	-600	0.53	No	
20070508 2101	18.9	1024	2048	No	0.51	566	178.4	924	-200	0.58	Yes	West
20070509 1042	22.3	1024	2048	No	0.51	890	331.0	924	-200	0.58	Yes	West
20070510 0603	31.0	1024	2048	No	0.51	447	230.4	-955	-100	0.56	Yes	East
20070511 0020	14.5	1024	1024	Yes	0.31	829	200.0	-15	1	1.55	No	
20070514 1121	5.0	512	1024	Yes	0.51	736	61.3	-30	929	0.59	Yes	North
20070514 1241	5.0	512	1024	Yes	0.51	463	38.6	-30	930	0.59	Yes	North
20070514 1324	5.0	512	1024	Yes	0.51	451	37.5	-960	0	0.56	Yes	East
20070514 1413	5.0	512	1024	Yes	0.51	850	70.9	-960	0	0.56	Yes	East
20070516 1058	5.0	512	1024	Yes	0.51	721	60.1	-30	929	0.59	Yes	North
20070516 1217	5.0	512	1024	Yes	0.51	435	36.3	-30	930	0.59	Yes	North
20070516 1258	5.0	512	1024	Yes	0.51	466	38.8	-960	0	0.56	Yes	East
20070516 1356	5.0	512	1024	Yes	0.51	758	63.2	-960	0	0.56	Yes	East
20070517 1439	9.6	1024	2048	No	0.31	454	72.3	-416	53	1.13	No	
20070521 1115	5.0	512	1024	Yes	0.51	396	33.0	-30	929	0.59	Yes	North
20070521 1208	5.0	512	1024	Yes	0.51	740	61.7	-30	930	0.59	Yes	North
20070521 1347	5.0	512	1024	Yes	0.51	916	76.4	-960	0	0.56	Yes	East
20070523 0557	15.3	1024	1024	Yes	0.31	1048	266.9	731	29	0.80	No	
20070523 1205	10.0	1024	1024	Yes	0.31	335	55.7	765	17	0.76	No	
20070523 1329	10.0	1024	1024	Yes	0.31	422	70.2	772	17	0.76	No	
20070523 1830	10.0	1024	1024	Yes	0.31	390	64.9	798	16	0.73	No	

Date/time	Cad.	nx	ny	Sum.	exp	nexp	Min.	x	y	mu	Limb	Orien.
20070523 2003	10.0	1024	1024	Yes	0.31	422	70.2	806	15	0.72	No	
20070523 2321	4.8	1024	1024	No	0.51	501	39.9	821	14	0.70	No	
20070524 0624	10.0	1024	1024	Yes	0.31	244	40.5	852	12	0.67	No	
20070524 0733	10.0	1024	1024	Yes	0.31	421	70.0	856	12	0.67	No	
20070524 0911	10.0	1024	1024	Yes	0.31	377	762.7	863	12	0.66	No	
20070525 0633	4.8	1024	1024	No	0.51	865	69.0	925	6	0.59	Yes	West
20070525 0811	4.8	1024	1024	No	0.51	875	69.8	928	5	0.59	Yes	West
20070525 1143	5.0	512	1024	Yes	0.51	659	54.9	-30	929	0.59	Yes	North
20070525 1306	5.0	512	1024	Yes	0.51	395	32.9	-30	929	0.59	Yes	North
20070525 1344	5.0	512	1024	Yes	0.51	390	32.5	-960	0	0.56	Yes	East
20070525 1445	5.0	512	1024	Yes	0.51	652	54.4	-960	0	0.56	Yes	East
20070529 1120	20.9	1024	1024	Yes	0.15	630	218.7	960	0	0.56	Yes	West
20070530 1134	5.0	512	1024	Yes	0.51	661	55.1	-30	929	0.59	Yes	North
20070530 1252	5.0	512	1024	Yes	0.51	450	37.5	-30	929	0.59	Yes	North
20070530 1334	5.0	512	1024	Yes	0.51	401	33.4	-960	0	0.56	Yes	East
20070530 1433	5.0	512	1024	Yes	0.51	670	55.9	-960	0	0.56	Yes	East
20070601 1809	8.0	512	1024	Yes	0.15	214	28.4	-465	-226	1.02	No	
20070601 1908	8.0	512	1024	Yes	0.15	509	67.8	-458	-226	1.03	No	
20070601 2047	8.0	512	1024	Yes	0.15	318	42.3	-445	-226	1.04	No	
20070603 1845	5.0	512	1024	Yes	0.51	806	67.2	-30	929	0.59	Yes	North
20070603 2023	7.1	512	1024	Yes	0.51	870	103.2	-960	0	0.56	Yes	East
20070615 1144	6.9	512	1024	Yes	0.51	1000	115.5	-30	929	0.59	Yes	North
20070615 1345	8.1	512	1024	Yes	0.51	847	114.5	-960	0	0.55	Yes	East

Date/time	Cad.	nx	ny	Sum.	exp	nexp	Min.	x	y	mu	Limb	Orien.
20070621 1058	6.9	512	1024	Yes	0.51	1000	115.5	-30	930	0.59	Yes	North
20070621 1258	7.2	512	1024	Yes	0.51	866	104.4	-960	0	0.55	Yes	East
20070630 1813	6.9	512	1024	Yes	0.51	1006	115.5	-30	929	0.59	Yes	North
20070630 2013	7.2	512	1024	Yes	0.51	885	105.4	-960	0	0.55	Yes	East
20070701 2130	7.0	512	1024	Yes	0.51	1878	220.0	-950	-99	0.56	Yes	East
20070702 2104	5.0	512	1024	Yes	0.51	370	30.8	-950	-100	0.56	Yes	East
20070702 2206	5.0	512	1024	Yes	0.51	805	67.1	-950	-100	0.56	Yes	East
20070702 2345	5.0	512	1024	Yes	0.51	806	67.2	-950	-99	0.56	Yes	East
20070703 2245	6.4	512	1024	Yes	0.51	1305	140.0	-932	-100	0.58	Yes	East
20070708 2003	5.0	512	1024	Yes	0.51	261	21.7	-30	929	0.59	Yes	North
20070708 2056	5.0	512	1024	Yes	0.51	759	63.3	-30	929	0.59	Yes	North
20070708 2234	5.0	512	1024	Yes	0.51	811	67.6	-960	0	0.55	Yes	South
20070717 0113	6.7	512	1024	Yes	0.51	991	111.3	-82	929	0.58	Yes	North
20070718 1140	10.9	1024	1024	No	0.21	1168	211.9	882	-127	0.63	No	
20070723 1352	8.0	1024	1024	No	0.21	539	71.8	-957	27	0.56	Yes	East
20070724 0122	8.0	1024	1024	No	0.21	540	71.9	-27	932	0.58	Yes	North
20070724 1128	11.5	1024	1024	No	0.21	814	155.5	935	100	0.58	Yes	West
20070724 1429	10.2	1024	1024	No	0.21	1415	239.9	935	100	0.58	Yes	West
20070725 0035	6.7	512	1024	Yes	0.51	1079	119.5	15	929	0.59	Yes	North
20070725 0234	6.2	512	1024	Yes	0.51	1320	135.3	-914	0	0.60	No	
20070725 0654	9.6	1024	1024	No	0.21	456	72.7	15	929	0.59	Yes	North
20070725 0832	8.0	1024	1024	No	0.21	484	64.4	15	929	0.59	Yes	North
20070725 2319	8.0	1024	1024	No	0.21	550	73.2	-854	-200	0.64	No	

Date/time	Cad.	nx	ny	Sum.	exp	nexp	Min.	x	y	mu	Limb	Orien.
20070728 0952	6.5	512	1024	Yes	0.51	905	98.6	-56	930	0.58	Yes	North
20070808 1053	5.0	512	1024	Yes	0.51	1385	115.5	0	929	0.59	Yes	North
20070808 1252	5.0	512	1024	Yes	0.51	1390	116.0	-929	0	0.59	Yes	East
20070808 1804	10.0	1024	1024	Yes	0.41	1411	235.1	-625	725	0.56	Yes	North-east
20070809 1715	10.0	1024	1024	Yes	0.41	1705	284.1	-639	698	0.57	Yes	North-east
20070820 1628	4.8	1024	1024	Yes	0.51	3019	241.1	-944	0	0.58	Yes	East
20070821 0130	4.8	1024	1024	Yes	0.51	1048	83.6	945	0	0.57	Yes	West
20070821 0254	4.8	1024	1024	Yes	0.51	444	35.4	944	0	0.58	Yes	West
20070821 1335	4.8	1024	1024	Yes	0.51	2555	204.0	945	0	0.57	Yes	West
20071013 2204	10.0	1024	1024	Yes	0.31	1053	175.4	945	0	0.59	Yes	West
20071027 1149	15.1	1024	1024	Yes	0.61	470	117.8	939	-100	0.59	Yes	West
20071107 1830	5.0	1024	1024	Yes	0.61	673	56.0	97	940	0.59	Yes	North
20071108 1830	5.0	1024	1024	Yes	0.61	709	59.0	97	940	0.60	Yes	North
20071110 0116	5.0	1024	1024	Yes	0.61	666	55.4	229	915	0.60	Yes	North
20071110 0340	5.0	1024	1024	Yes	0.61	474	39.4	230	915	0.60	Yes	North
20071110 0515	5.0	1024	1024	Yes	0.61	500	41.6	229	915	0.60	Yes	North/North-west
20071110 0700	5.0	1024	1024	Yes	0.61	954	79.4	230	915	0.60	Yes	North/North-west
20071120 1103	6.0	1024	2048	Yes	0.51	3980	398.0	961	110	0.57	Yes	West
20071120 1756	6.0	1024	2048	Yes	0.51	3635	363.5	961	110	0.57	Yes	West

Table B.1: Data sets satisfying the requirements in Section 3.4. The table is showing the date/time, cadence, pixel span in x and y directions respectively, whether the data is summed (2x2 pixels) or not, exposure time, number of exposures, time span in minutes, the distance from the solar center to the central pixel in FoV in x and y direction respectively, the $\mu = \cos\theta$, whether the time series is on the limb and if it is on the limb; in which direction.

Bibliography

Balthasar, H., von der Luhe, O., Kneer, F., Staude, J., Volkmer, R., Berkefeld, T., Caligari, P., Collados, M., Halbgewachs, C., Heidecke, F., Hofmann, A., Klvana, M., Nicklas, H., Popow, E., Puschmann, K., Schmidt, W., Sobotka, M., Soltau, D., Strassmeier, K., and Wittmann, A. (2007). GREGOR: The new German Solar Telescope. In Heinzel, P., Dorotovic, I., and Rutten, R. J., editors, *The Physics of Chromospheric Plasmas*, volume 368 of *ASP Conerence Series*, pages 605–610.

Barthol, P., Gandorfer, A., Solanki, S., Knolker, M., Pillet, V. M., Schmidt, W., Title, A., and the SUNRISE team (2008). SUNRISE: High resolution UV/VIS observations of the sun from the stratosphere. *Advances in Space Research*, 42:70–77.

Beckers, J. (1968). Solar Spicules. *Solar Physics*, 3:367–433.

Bel, N. and Leroy, B. (1977). Analytical study of magneto-acoustic gravity waves. *Astronomy and Astrophysics*, 55:239–243.

Brault, J. and Neckel, H. (1987). Spectral atlas of solar disk-averaged and disk-center intensity from 3290 to 12510 aa. *Hamburg Observatory anonymous ftp:* `ftp.hs.uni-hamburg.de`.

Carlsson, M. (1986). A computer program for solving multi-level non-LTE radiative transfer problems in moving or static atmospheres. *Uppsala Astronomical Observatory Report*, 33.

Carlsson, M., Hansteen, V. H., de Pontieu, B., McIntosh, S., Tarbell, T. D., Shine, D., Tsuenta, S., Katsuwaka, Y., Ichimoto, K., Suematsu, Y., Shimizu, T., and Nagata, S. (2007). Can high frequency acoustic waves heat the quiet Sun chromosphere? *Publ. Astronomical Society Japan*, 59:663 – 668.

Carroll, B. and Ostlie, D. (1996). *An Introduction to Modern Astrophysics*. Pearson, Addison Wesley.

De Pontieu, B., Erdelyi, R., and James, S. P. (2004). Solar chromospheric spicules from the leakage of photospheric oscillations and flows. *Nature*, 430.

De Pontieu, B., Hansteen, V. H., van der Voort, L. R., van Noort, M., and Carlsson, M. (2007a). High-resolution observations and modelling of dynamic fibrils. *The Astrophysical Journal*, 655:624–641.

De Pontieu, B., McIntosh, S., Hansteen, V., Carlsson, M., Schrijver, C., Tarbell, T., Title, A., Shine, R., Suematsu, Y., Tsuneta, S., Katsukawa, Y., Ichimoto, K., Shimizu, T., and Nagata, S. (2007b). A Tale of Two Spicules: The Impact of Spicules on the Magnetic Chromosphere. *Publ. Astron. Soc. Japan (PASJ)*, 59:655–662.

Fontenla, J. M., Avrett, E. H., and Loeser, R. (1990). Energy balance in the solar transition region. I - Hydrostatic thermal models with ambipolar diffusion. *The Astrophysical Journal*, 355:700–718.

Foukal, P. V. (2004). *Solar Astrophysics*. WILEY–VCH, 2nd edition.

Gumley, L. E. (2002). *Practical IDL programming*. Morgan Kaufmann Publishers.

Hansteen, V., de Pontieu, B., van der Voort, L. R., van Noort, M., and Carlsson, M. (2006). Dynamic fibrils are driven by magnetoacoustic shocks. *The Astrophysical Journal*, 647:L73–L76.

Hasan, S. (2008). Chromospheric Dynamics. *Advances in Space Research*, 42:86–95.

Heggland, L., de Pontieu, B., and Hansteen, V. H. (2007). Numerical simulations of shock wave-driven chromospheric jets. *The Astrophysical Journal*, 666:1277–1283.

Howell, S. B. (2000). *Handbook of CCD Astronomy*. Cambridge.

Hurlburt, N., Slater, G., Tarbell, T., Berger, T., and Katsukawa, Y. (2007). Hinode Solar Optical Telescope Data Analysis Guide. From website: http://hinode.nao.ac.jp/hsc_e/analysis_e.shtml.

Ichimoto, K. and team, H. (2007). Solar Optical Telescope onboard Hinode for Diagnosing the Solar Magnetic Fields. *Plasma and Fusion Research*, 2:S1009–S1009.

Ikhsanov, R. and Ivanov, V. (1999). Properties of space and time distribution of solar coronal holes. *Solar Physics*, 188:245–258.

Judge, P. (2006). Observations of the solar chromosphere. In Uitenbroek, Leibacher, and Stein, editors, *Solar MHD theory and observations: A high spatial resolution perspective*, volume 354 of *ASP Conference Series*, pages 259 – 275.

Kosugi, T., Matsuzaki, K., Sakao, T., Shimizu, T., Sone, Y., Tachikawa, S., Hashimoto, T., Minesugi, K., Ohnishi, A., Yamada, T., Tsuneta, S., Hara, H., Ichimoto, K., Suematsu, Y., Shimojo, M., Watanabe, T., Shimada, S., Davis, J., Hill, L., Owens, J., Title, A., Culhane, J., Harra, L., Doschek, G., and Golub, L. (2007). The Hinode (Solar-B) Mission: An Overview. *Solar Physics*, I(243):3–17.

Leung, C. M. (2006). Radiative Transfer. In *Encyclopedia of Astronomy & Astrophysics*. IOP Publishing Ltd.

Magain, P. (1986). Contribution functions and the depths of formation of spectral lines. *Astronomy and Astrophysics*, 163:135–139.

Marsden, R. G. and Fleck, B. (2007). Solar ORBITER: A mission update. In Heinzel, P., Dorotovic, I., and Rutten, R. J., editors, *The Physics of Chromospheric Plasmas*, volume 368 of *ASP Conference Series*, pages 645–652. ESA, ESTEC.

Michalitsanos, A. (1973). The five-minute period oscillation in magnetically active regions. *Solar Physics*, 30:47–61.

Mihalas, D. and Weibel-Mihalas, B. (1999). *Foundations of radiation hydrodynamics*. Dover, 2nd edition.

Rimmele, T. and the ATST team (2008). The unique scientific capabilities of the Advanced Technology Solar Telescope. *Advances in Space Research*, 42:78–85.

Stix, M. (2002). *The Sun, An Introduction*. Springer, 2 edition.

Suematsu, Y. (1990). Influence of photospheric 5-minute oscillations on the formation of chromospheric fine structures. In Osaki, Y. and Shibahashi, H., editors, *Progress of seismology of the Sun and stars*, volume 367 of *Lecture notes in physics, Proceedings of the Oji international seminar*, pages 211–214. Springer-Verlag.

Tsuneta, S., Ichimoto, K., Katsukawa, Y., Nagata, S., Otsubo, M., Shimizu, T., Suematsu, Y., Nakagiri, M., Noguchi, M., Tarbell, T., Title, A., Shine, R., Rosenberg, W., Hoffmann, C., Jurcevich, B., Kushner, G., Levay, M., Lites, B., Elmore, D., Matsushita, T., Kawaguchi, N., Saito, H., Mikami, I., Hill, L., and Owens, J. (2007). The Solar Optical Telescope for the Hinode Mission: An Overview. submitted.

Vernazza, J., Avrett, E., and Loeser, R. (1981). Structure of the solar chromosphere, III. Models of the EUV brightness components of the quiet sun. *The Astrophysical Journal supplement series*, 45:635 – 725.

Øivind Wikstøl (2006). Data processing, AST5120 lecture notes.